Novel Roles of the N1 Loop and N4 Alpha-Helical Region of the Nipah Virus Fusion Glycoprotein in Modulating Early and Late Steps of the Membrane Fusion Cascade

J. Lizbeth Reyes Zamora,[a] Victoria Ortega,[a] Gunner P. Johnston,[a] Jenny Li,[a] [ID]Hector C. Aguilar[a]

[a]Department of Microbiology and Immunology, College of Veterinary Medicine, Cornell University, Ithaca, New York, USA

ABSTRACT Nipah virus (NiV) is a zoonotic bat henipavirus in the family *Paramyxoviridae*. NiV is deadly to humans, infecting host cells by direct fusion of the viral and host cell plasma membranes. This membrane fusion process is coordinated by the receptor-binding attachment (G) and fusion (F) glycoproteins. Upon G-receptor binding, F fuses membranes via a cascade that sequentially involves F-triggering, fusion pore formation, and viral or genome entry into cells. Using NiV as an important paramyxoviral model, we identified two novel regions in F that modulate the membrane fusion cascade. For paramyxoviruses and other viral families with class I fusion proteins, the heptad repeat 1 (HR1) and HR2 regions in the fusion protein prefusion conformation bind to form a six-helix bundle in the postfusion conformation. Here, structural comparisons between the F prefusion and postfusion conformations revealed that a short loop region (N1) undergoes dramatic spatial reorganization and a short alpha helix (N4) undergoes secondary structural changes. The roles of the N1 and N4 regions during the membrane fusion cascade, however, remain unknown for henipaviruses and paramyxoviruses. By performing alanine scanning mutagenesis and various functional analyses, we report that specific residues within these regions alter various steps in the membrane fusion cascade. While the N1 region affects early F-triggering, the N4 region affects F-triggering, F thermostability, and extensive fusion pore expansion during syncytium formation, also uncovering a link between F-G interactions and F-triggering. These novel mechanistic roles expand our understanding of henipaviral and paramyxoviral F-triggering, viral entry, and cell-cell fusion (syncytia), a pathognomonic feature of paramyxoviral infections.

IMPORTANCE Henipaviruses infect bats, agriculturally important animals, and humans, with high mortality rates approaching ~75% in humans. Known human outbreaks have been concentrated in Southeast Asia and Australia. Furthermore, about 20 new henipaviral species have been recently discovered in bats, with geographical spans in Asia, Africa, and South America. The development of antiviral therapeutics requires a thorough understanding of the mechanism of viral entry into host cells. In this study, we discovered novel roles of two regions within the fusion protein of the deadly henipavirus NiV. Such roles were in allowing viral entry into host cells and cell-cell fusion, a pathological hallmark of this and other paramyxoviruses. These novel roles were in the previously undescribed N1 and N4 regions within the fusion protein, modulating early and late steps of these important processes of viral infection and henipaviral disease. Notably, this knowledge may apply to other henipaviruses and more broadly to other paramyxoviruses.

KEYWORDS F-triggering, FG interactions, Nipah, entry, fusion, henipavirus, paramyxovirus

Nipah virus (NiV) and related henipaviruses are considered by the World Health Organization (WHO) as top priority pathogens with high epidemic risk to humans
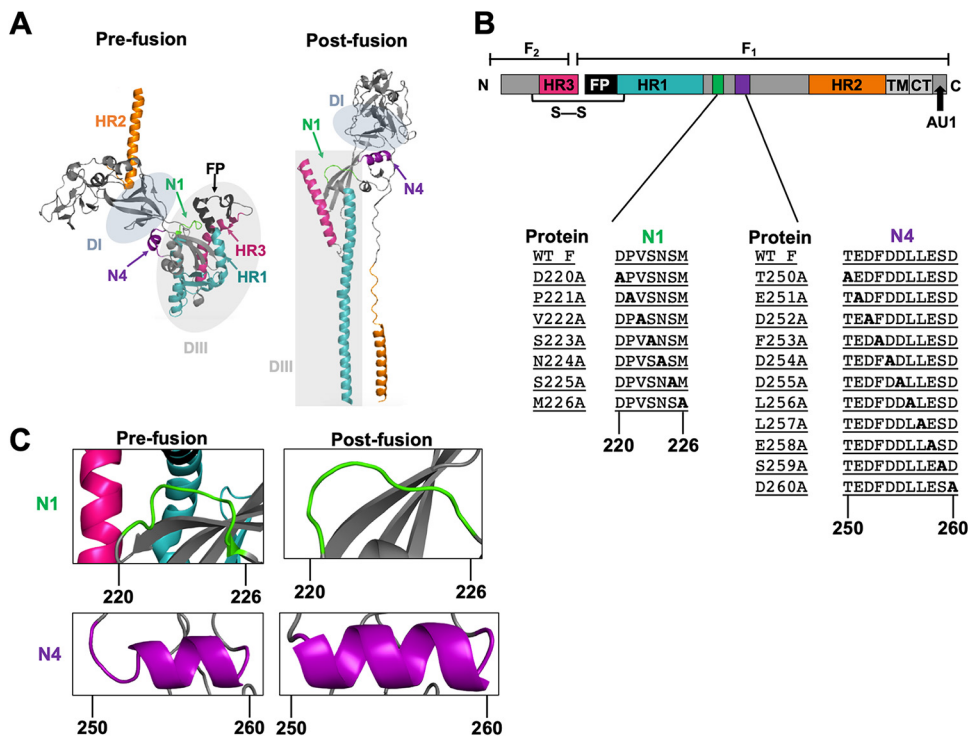
FIG 1 Differences in spatial arrangements and secondary structures of the N1 and N4 regions between the pre- and postfusion conformations. (A) NiV F published prefusion and modeled postfusion monomer. The heptad repeats HR1 and -2 are highlighted in teal and orange, respectively. HR3 is highlighted in magenta. The N1 and N4 regions are highlighted in green and purple, respectively. The fusion peptide is shown in black. Areas shaded in gray denote the previously described DI and DIII domains (30, 31, 34). (B) Schematic of the NiV F protein. The green and purple areas denote the N1 and N4 regions, respectively. The N1 and N4 inserts show the native amino acid sequences as well as the scanning alanine mutants constructed in residues 220 to 226 and 250 to 260, respectively. WT, wild type. (C) Close-ups of spatial and/or secondary structural changes observed in the pre- and postfusion conformations of the N1 region in green and the N4 region in purple.

(1). Similarly to other paramyxoviruses, NiV is highly infectious, primarily infecting the respiratory tract and the central nervous system. NiV in particular typically causes brain inflammation, severe respiratory syndrome, and vasculitis and has an average mortality rate in humans of 75%, reaching 90 to 100% in some outbreaks (2–6). Despite the importance of NiV, there are still no approved therapeutic countermeasures or vaccines available for human use (7, 8). A clearer understanding of the mechanism of viral entry into host cells is crucial to the development of such therapeutics.

Paramyxoviral entry occurs through a virus-cell membrane fusion process that is driven by two surface proteins: the attachment (HN, N, or G) and fusion (F) glycoproteins. The attachment glycoprotein sequences differ relatively more among paramyxoviruses, binding various host cell receptors and being designated HN, H, or G (9–17). The fusion glycoprotein (F) is relatively more structurally and functionally conserved. F ultimately fuses the viral and host cell membranes during viral entry or cell-cell membrane fusion (syncytium formation), a pathognomonic feature of paramyxoviral infections (9–13, 18). The class I fusion protein NiV F is initially synthesized as an inactive precursor (F_0) that is cleaved within an endocytic compartment by cathepsin L into two disulfide-linked subunits, F_1 and F_2 (19–21). Processed F contains a new N-terminal hydrophobic fusion peptide (FP) (Fig. 1B). Downstream of the FP are the archetypical heptad repeat (HR) helical regions (designated HR1 and HR2) (Fig. 1B). As NiV G engages its ephrin B2 receptor, G undergoes conformational changes that trigger NiV F conformational changes, resulting in FP insertion into the target cell membrane, fully extending the HR1 region and forming the transient pre-hairpin intermediate (PHI) (22–24). HR1 and HR2 refolding and binding form the energetically stable postfusion

six-helix bundle (6HB), causing the viral and host cell membranes to mix and ultimately fuse (18, 24–27).

The pre- and postfusion structures of several paramyxoviral F glycoproteins have been previously solved (28–34). These structures bring to light some well-characterized and some less-understood differences between the pre- and postfusion F conformations. Specifically, the HR1 and HR2 regions have been studied extensively, and rearrangements between the HR1 and HR2 regions between the prefusion and postfusion F conformations are widely accepted as a main driver of membrane fusion (9–13, 24–27, 35–37). Furthermore, we recently showed the role of a third large helical domain, termed HR3, in modulating early F-triggering and late steps of the membrane fusion cascade (38). However, other molecular rearrangements that occur between the transitional conformational states of F and their role in the membrane fusion cascade remain largely enigmatic for the henipaviruses and paramyxoviruses.

In the first paramyxoviral F crystal structure, that of the Newcastle disease virus (NDV) postfusion F conformation (29), four short helices downstream of the HR1 region were designated N1, N2, N3, and N4. The solved parainfluenza virus 5 (PIV5) W3A processed prefusion F (PDB accession code 4GIP), as well as the PIV5 WR strain prefusion F (PDB accession code 4WSG), similarly contained the four short helices N1 to N4 (31, 33). In the recently solved NiV prefusion F structure (PDB accession code 5EVM), the N1 region exists as a linker, as opposed to an alpha helix (as in NDV and PIV5 F), followed by three small helices—N2, N3, and N4 (28). Notably, when we compared the prefusion structure of NiV F with a postfusion NiV F modeled after human parainfluenza virus 3 (hPIV3), we observed a large spatial displacement of the N1 region (Fig. 1A). In the prefusion NiV F conformation, the N1 region is in close association with the FP, as well as HR1 and HR3 (regions involved in F-triggering). In the postfusion conformation, this close association is lost (Fig. 1A and C). On the other hand, in the prefusion conformation, the N4 region is at an interface between domains DI (containing β-sheets) and DIII (which contains the HR1, HR3, and FP). In the postfusion conformation, the DI and DIII domains are now rotated around N4 and the N4 region gains an additional helical turn (Fig. 1A and C). Moreover, the primary sequence, location, and configuration of the N1 and N4 regions are well conserved among henipaviruses and paramyxoviruses (see Fig. 9 below). For these reasons, we hypothesized that the N1 and N4 regions are important in releasing the fusion peptide and aiding transition into the PHI (hereby termed F-triggering).

To investigate the roles of the N1 and N4 regions, we performed a comprehensive alanine scanning mutagenesis spanning these regions, covering individual residues 220 to 226 and 250 to 260, respectively (Fig. 1B). We first tested these alanine mutants for their levels of cell surface expression (CSE), total cell expression, processing, gross prefusion conformational states, and syncytial fusion assays. We then further tested specific mutants of interest shown to affect the membrane fusion process in functional F-triggering, fusion pore formation (dual split protein [DSP] assays), viral entry assays, and F-G interaction assays (coimmunoprecipitation [co-IP] assays). As we had hypothesized, our studies uncovered point mutants in these regions that affected early F-triggering steps of the membrane fusion cascade. Furthermore, our results uncovered that the N4 region modulated not only F-triggering, but also later steps during the membrane fusion cascade, such as fusion pore expansion, as well as thermostability of the F protein. Importantly, these studies uncovered a strong inverse relationship between F-G interactions and F-triggering. These results shed light on the modulation of multiple steps in the NiV membrane fusion cascade, uncovering two novel fusion-modulatory regions in F, with likely mechanistic implications for other henipaviruses' and paramyxoviruses' fusion processes.

RESULTS

Structural comparisons of the NiV F prefusion versus postfusion conformations reveal spatial rearrangements around the N1 and N4 regions, as well as secondary structural changes in the N4 region. NiV F is a trimeric class I fusion protein that contains two helical heptad repeats, HR1 (in teal) and HR2 (in orange) (Fig. 1A and B). The

prefusion conformation of NiV F has been recently solved (PDB ID accession code 5EVM [Fig. 1A, left]) (28). As F progresses through the fusion cascade, F goes from the metastable prefusion to the highly stable postfusion conformation, both shown as F monomers (Fig. 1A). A crystal structure for the postfusion NiV F remains to be solved; therefore, we generated an NiV F postfusion monomer model using SWISS-MODEL with the existing hPIV3 F X-ray crystal structure, which is 30% identical in primary sequence to NiV F (PDB ID accession code 1ZTM [Fig. 1A, right]) (30, 39–42). Structural analysis of the published prefusion NiV F monomer showed the N1 region (in green) in close association with the fusion peptide (FP), HR1, and HR3 (magenta). Contrarily, the postfusion NiV F model conformation depicted the N1 region as no longer in close association with the FP, HR1 and HR3 (Fig. 1C). Structural analysis of the N4 region (in purple) in the prefusion conformation showed N4 is initially located at an interface between the DI domain (containing β-sheets) and the DIII domain (which contains the FP, HR1, and HR3). In contrast, in the postfusion conformation, these DI and DIII domains have now rotated around N4, and an additional helical turn is gained by N4 (Fig. 1A and C). Due to these observations, we hypothesized that the N1 and N4 regions are important in modulating the membrane fusion cascade, particularly at the early F-triggering step(s). To elucidate the functionality of these regions in the membrane fusion process, we performed alanine scanning mutagenesis in the N1 (amino acids 220 to 226 [aa 220–226]) and N4 (aa 250–260) regions (Fig. 1B).

NiV F N1 and N4 regions contain select mutants with hypo- or hyperfusogenic phenotypes, despite wild-type levels of cell surface expression. We first tested the capacity of the N1 and N4 NiV F mutants to induce cell-cell fusion. HEK 293T cells were transfected with wild-type NiV G and either wild-type or mutant NiV F. After 12 to 16 h posttransfection, cells were fixed, and nuclei inside fused cells (syncytia) were quantified by microscopic analysis. Several mutants with mutations in the N1 region showed significant differences in syncytium formation: D220A ($\sim$60%, $P \leq 0.05$), P221A ($\sim$20%, $P \leq 0.01$), V222A ($\sim$0%, $P \leq 0.0001$), and M226A ($\sim$0%, $P \leq 0.0001$). Two mutants had significantly increased fusion levels: S223A ($\sim$230%, $P \leq 0.01$) and N224A ($\sim$200%, $P \leq 0.05$) (Fig. 2A). Furthermore, the majority of the N4 region mutants showed significantly decreased syncytial fusion levels: T250A ($\sim$60%, $P \leq 0.05$), D252A ($\sim$1%, $P \leq 0.0001$), F253A ($\sim$0%, $P \leq 0.0001$), D255A ($\sim$4%, $P \leq 0.0001$), L256A ($\sim$1%, $P \leq 0.0001$), and E258A ($\sim$0%, $P \leq 0.0001$) (Fig. 2C). Interestingly, however, two of the 11 N4 mutants showed highly significantly increased fusion levels, with the L257A mutant yielding $\sim$600% fusion ($P \leq 0.0001$) and the S259A mutant having $\sim$280% fusion ($P \leq 0.001$) compared to wild-type NiV F (Fig. 2C).

Since we and others have shown that cell-cell fusion levels are dependent on cell surface expression levels of the henipaviral glycoproteins (43, 44), to verify that the cell-cell fusion phenotypes were not due to differences in cell surface expression levels of the mutant proteins, we expressed N1 or N4 NiV F mutants in HEK 293T cells and measured relative cell surface expression by flow cytometric analyses as normalized to wild-type NiV F. The P221A, S223A, and N224A N1 region mutants were expressed at the cell surface at levels comparable to wild-type NiV F (Fig. 2A). The N1 NiV F D220A, V222A, and M226A mutants yielded significantly to highly significantly lower levels of cell surface expression (Fig. 2A). The extremely low levels of CSE of N1 V222A and M226A mutants explain the observed lack of syncytia (Fig. 2A). Fusion index scores were then calculated by dividing the normalized percentage of syncytia by the normalized percentage of cell surface expression to account for the effects of cell surface expression of F on syncytium formation, as per several prior publications (43, 45, 46). These fusion index calculations revealed that P221A, S223A, and N224A mutants had significant differences in fusion index scores ($P \leq 0.05$) (Fig. 2B). Thus, of the NiV F N1 region alanine point mutants, these three mutants displayed differences in their inherent fusogenic capacities.

A similar analysis was carried out for the N4 alanine point mutants. The N4 T250A, E251A, D254A, D255A, L256A, L257A, E258A, S259A, and D260A mutants were all expressed at the cell surface at levels comparable to wild-type NiV F (Fig. 2C). The
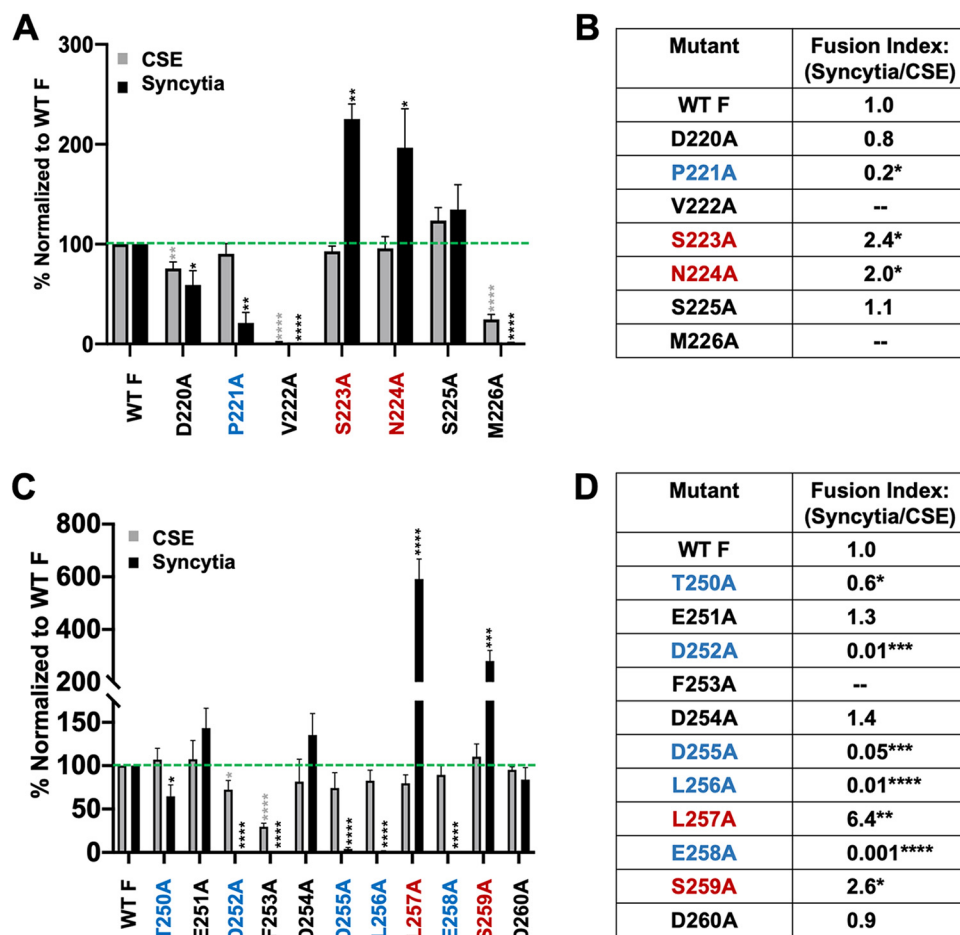
FIG 2 Cell-surface expression, syncytial formation, and fusion indices of N1 and N4 region mutants. (A) Relative levels of cell surface expression (CSE; gray) and syncytium formation (black) of NiV F N1 mutants normalized to wild-type (WT) NiV F. (B) Fusion indices determined by dividing normalized percentage of syncytia by normalized percentage of CSE for the N1 region mutants. (C) Relative levels of CSE (gray) and syncytium formation (black) for the NiV F N4 mutants normalized to wild-type NiV F. (D) Fusion indices determined by dividing the normalized percentage of syncytia by the normalized percentage of CSE for the N4 region mutants. The green dashed line represents wild-type levels of CSE and syncytia. Results are averages from at least five experiments, with error bars indicating standard error of the mean. Statistically significant differences, as determined by a one-sample Student's t test, are marked with asterisks: *, $P \leq 0.05$; **, $P \leq 0.01$; ***, $P \leq 0.001$; and ****, $P \leq 0.0001$.

F253A mutant had a severely decreased level of cell surface expression, which likely accounted for the lack of syncytia observed (Fig. 2C). Although the N4 region D252A mutant had ∼72% CSE levels ($P \leq 0.0001$), there was a markedly absent level of syncytia observed. Furthermore, when we calculated their fusion index scores, T250A, D252A, D255A, L256A, and E258A mutants were all significantly hypofusogenic, while L257A and S259A mutants were significantly hyperfusogenic (Fig. 2C and D). Therefore, we further pursued our functional analyses of these seven fusion mutants within the N4 region. It was remarkable that the relatively small N4 region contained seven cell-cell fusion mutants within a stretch of 10 residues (70%).

F processing levels of the N1 and N4 region mutants are not significantly affected. NiV F requires endocytic processing of the F_0 precursor by the endosomal cathepsin L for cleavage into the F_1/F_2 subunits and thus activation (19–21, 47). Because levels of F processing may affect the membrane fusion function of NiV F, we sought to determine whether the N1 and N4 region mutants yielded alterations in F processing. We observed no significant differences in processing efficiency between wild-type NiV F and N1 region mutants. Furthermore, the low cell surface expression of V222A and
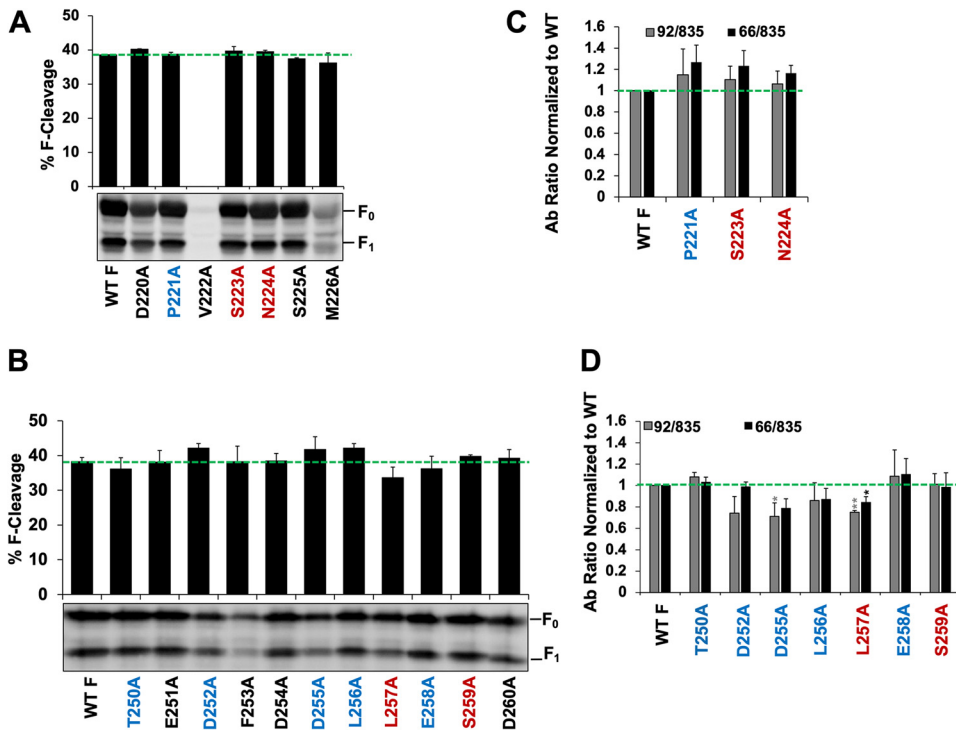
FIG 3 Levels of F processing and relative overall NiV F mutant prefusion conformations. (A and B) Levels of F processing determined by quantitative Western blotting (using detection of fluorescent antibodies) of cell lysates from NiV F N1 mutants (A) or (B) NiV F N4 mutants. Levels of processing were determined by dividing the F_1 signal by total $F_0 + F_1$ in cell lysates. The average from three experiments is shown, with error bars indicating the standard error of the mean. Lack of statistically significant differences was determined by two-sample Student's t test. A representative image of total cell lysates is shown. (C and D) Relative levels of MAb 92 and 66 binding of wild-type NiV F or N1 region mutants (C) or (D) N4 region mutants, all normalized to those of wild-type NiV F. All antibody binding levels were normalized to the CSE of each N1/N4 NiV F (as measured by PAb 835 binding). $n = 3$. Statistically significant differences, as determined by a one-sample Student's t test, are marked with asterisks: *, $P \le 0.05$; **, $P \le 0.01$.

M226A mutants was corroborated by Western blotting (Fig. 3A). Of note, the V222A mutant yielded basically no NiV F expression. Similarly, N4 region mutants had wild-type levels of NiV F processing (Fig. 3B). The low cell surface expression level of the F253A mutant was also corroborated by Western blotting (Fig. 3B). Therefore, the large majority of the N1 and N4 region mutants had roughly wild-type levels of F processing.

Overall conformations of the N1 and N4 region fusion mutants are grossly similar to those of wild-type NiV F. We then asked whether mutations in the N1 region of NiV F resulted in changes in the gross prefusion F conformation. We previously produced two rabbit monoclonal antibodies (MAbs), 92 and 66, that bind distinct conformational epitopes (45). As recently reported, the binding epitope of MAb 66 is the apex end of the prefusion F protein (48). Therefore, relative binding levels of MAbs 92 and 66 to the wild type and N1 region mutants were measured by flow cytometric analyses. The binding ratios of F binding to MAbs 92 or 66 relative to polyclonal antiserum 835 (here, PAb 835), our overall NiV F expression control, were calculated to normalize for transfection efficiencies: MAb 92/PAb 835 and MAb 66/PAb 835, respectively (Fig. 3C). Although the N1 region mutants of interest appeared to have a slight increase in the level of binding to MAb 66, the differences in MAb 92/PAb 835 or MAb 66/PAb 835 antibody binding ratios were not statistically significant compared to those of wild-type NiV F (Fig. 3C). Hence, overall fusion mutants of interest in the N1 region did not significantly alter the F overall prefusion conformation. Similarly, five of seven N4 fusion mutants yielded no major differences in MAb 92/PAb 835 and MAb 66/PAb 835 antibody binding ratios compared to wild-type NiV F. While D252A, D255A, L256A,

and L257A mutants appeared to have slightly decreased levels of MAb 92 binding, only those of D255A and L257A mutants were statistically significant (Fig. 3D). Furthermore, while D255A, L256A, and L257A mutants appeared to have a slightly decreased level of binding to MAb 66, only that of the L257A mutant was statistically significant (Fig. 3D). Therefore, most of the mutations in the N4 region did not alter the F overall conformations, and two mutations altered them only slightly.

The N1 region modulates early F-triggering steps. Because of the observed proximity of the N1 region to the FP, HR1, and HR3 (Fig. 1A and C), we hypothesized this region would affect F-triggering. After confirming that the observed syncytial fusion phenotype was not due to defects in F processing or overall F conformational states, we performed functional F-triggering assays as previously described (38, 49–51). Briefly, the F-triggering assay is capable of quantifying NiV F entering the PHI conformation (a step we define as F-triggering). In the PHI, the FP is inserted into the opposing target membrane, and the HR1 region is fully extended and exposed, thus allowing the HR2-Cy5-labeled peptide to bind NiV F on the cell surface. The Cy5 signal is then detected and quantified by flow cytometric analysis. The hypofusogenic N1 P221A mutant yielded significantly reduced levels of F-triggering compared to the wild-type NiV F ($\sim$20%, $P \leq 0.001$). Conversely, the hyperfusogenic S223A and N224A mutants were triggered to higher levels compared to wild-type F ($\sim$1.5-fold, $P \leq 0.001$, and $\sim$2.5-fold, $P \leq 0.05$, respectively).

To determine if F triggering affected the subsequent post-F-triggering steps, we tested the N1 fusion mutants in previously described dual split protein (DSP) fusion pore formation assay adapted for NiV (37, 38, 49–52). Upon formation of a sufficiently sized fusion pore between effector and target cells, both portions of the green fluorescent protein (GFP)-*Renilla* luciferase dual split proteins (DSP$_{1-7}$ and DSP$_{8-11}$) combine to form a fully functional *Renilla* luciferase (as well as fluorescent GFP). Luciferase activity was then measured 8 h postoverlay and normalized to wild-type NiV F (set as 100%), as previously described (37, 38, 49, 52). The hypofusogenic P221A mutant yielded significantly decreased fusion pore formation versus DSP fusion ($\sim$60%, $P \leq 0.05$) compared to wild-type NiV F (Fig. 4A). Contrarily, the hyperfusogenic S223A and N224A mutants yielded $\sim$200% ($P \leq 0.01$) and $\sim$150% ($P \leq 0.01$) DSP fusion, respectively (Fig. 4A). Fusion pore formation levels overall reflected the F-triggering levels obtained for these mutants, suggesting that the N1 region affects the F-triggering step and consequently the downstream fusion pore formation and extensive fusion pore expansion steps that result in syncytium formation (Fig. 4A). We performed correlation studies between the levels of F-triggering and fusion pore formation for the N1 mutants (Fig. 4B), and we observed a direct correlation trend, although likely due to the low number of mutant data points for this region, the correlation was not statistically significant. However, when we graphed the N1 mutant data points collectively with N4 mutant data points (Fig. 4E and F), a significant positive correlation was observed, suggesting that the N1 region likely affects the early F-triggering step(s) and consequently the downstream fusion pore formation step(s).

The N4 region modulates early F-triggering steps, as well as a later fusion pore expansion step(s). Our F-triggering assays also revealed that the hypofusogenic N4 T250A ($\sim$60%, $P \leq 0.05$), D255A ($\sim$6%, $P \leq 0.01$), L256A (0%, $P \leq 0.0001$), and E258A ($\sim$4%, $P \leq 0.001$) mutants yielded the indicated significantly reduced levels of F-triggering compared to the wild-type NiV F (Fig. 4C). Conversely, the hyperfusogenic N4 L257A ($\sim$180%) and S259A ($\sim$230%) mutants were triggered to higher levels than wild-type NiV F ($P \leq 0.01$ [Fig. 4C]). Interestingly, the hypofusogenic D252A mutant had near wild-type levels of F-triggering, suggesting a post-F-triggering fusion phenotype for this mutant (Fig. 4C).

To determine if F-triggering levels affected the subsequent steps, we tested the N4 region fusion mutants via the aforementioned dual split protein fusion pore formation assay (38, 49–51). Interestingly, the T250A mutant yielded wild-type levels of fusion pore formation. The hypofusogenic D252A ($\sim$37%, $P \leq 0.05$), D255A ($\sim$20%, $P \leq 0.05$), L256A ($\sim$25%, $P \leq 0.001$), and E258A ($\sim$0.3%, $P \leq 0.0001$) mutants yielded the
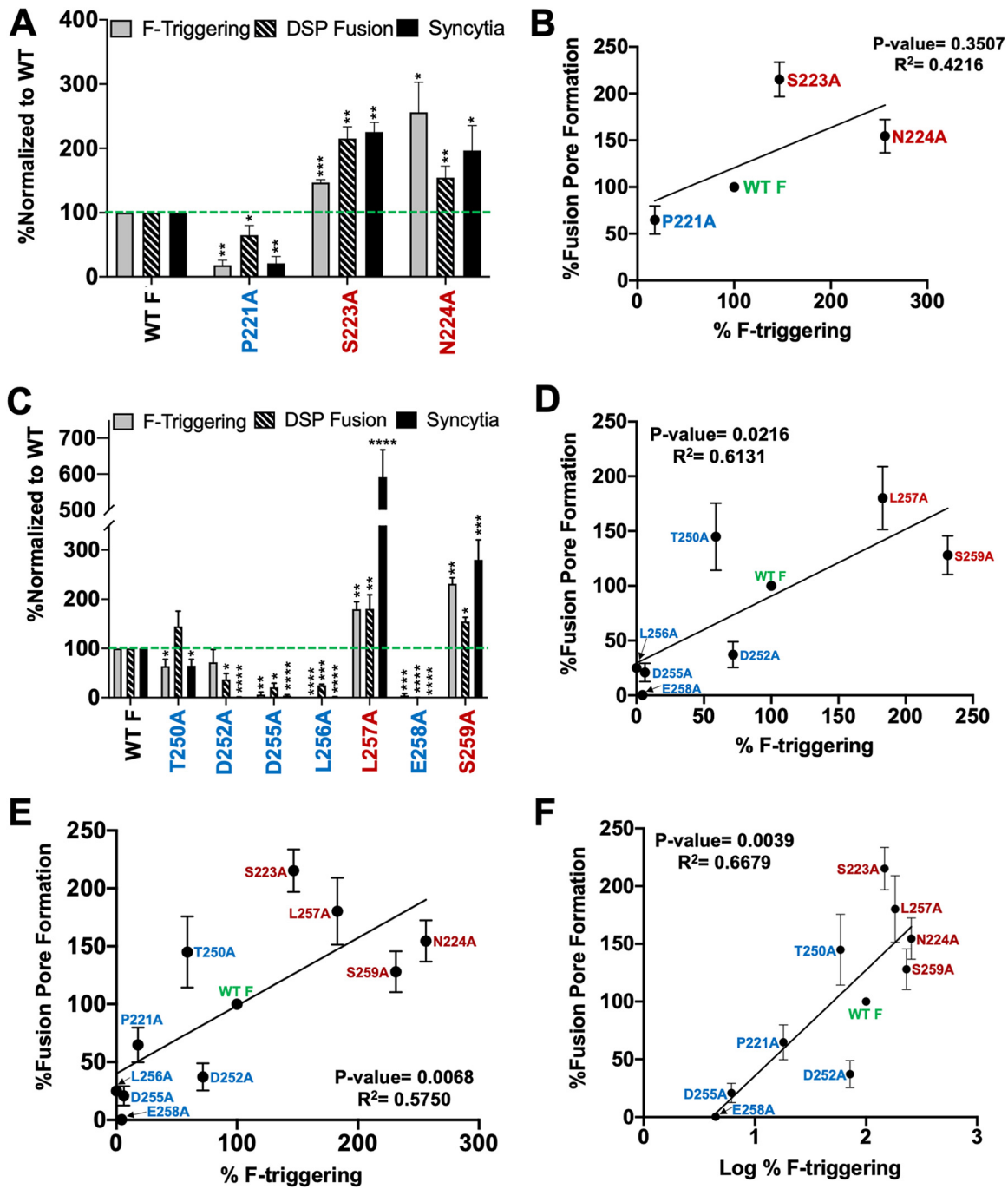
FIG 4 Positive correlation between F-triggering and fusion pore formation for the NiV F N1 and N4 region fusion mutants. (A and C) Levels of F-triggering and fusion pore formation of select NiV F N1 and N4 regions mutants compared to wild-type F in HEK 293T cells. F-triggering levels were determined by flow cytometry using a Cy5-labeled HR2 peptide and normalized to CSE levels for each mutant. Dual split protein fusion assay results (fusion pore formation) were normalized to wild-type NiV F. Levels of F-triggering, DSP fusion, and syncytium formation (from Fig. 2A) are shown together to better illustrate the step(s) of fusion affected. The data shown are averages from at least 3 experiments, with error bars indicating standard error of the mean. Statistically significant differences, as determined by a one-sample Student's t test, are marked with asterisks: *, $P \leq 0.05$; **, $P \leq 0.01$; ***, $P \leq 0.001$; and ****, $P \leq 0.0001$. (B) Percentage of fusion pore formation plotted against percentage of F-triggering from panel A. (D) Percentage of fusion pore formation plotted against percentage of F-triggering from panel C. (E) Percentage of fusion pore formation plotted against percentage of F-triggering of both N1 and N4 mutants from panels A and C. (F) Percentage of fusion pore formation plotted against log percentage of F-triggering of both N1 and N4 mutants from panels A and C. Note that the L256A mutant was excluded from the analysis as the log of 0% F-triggering is undefined.
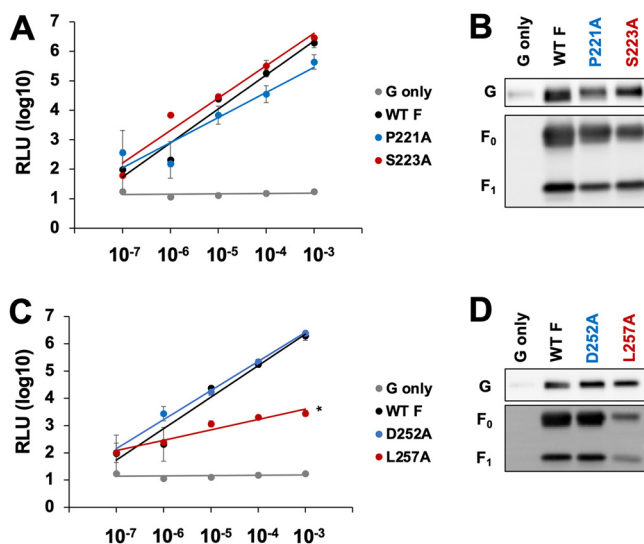
FIG 5 Infectivity of NiV F N1 and N4 region mutants. (A and C) Viral entry of NiV/VSV pseudotyped virions expressing NiV F (wild type or N1 or N4 region mutants) over serial dilutions of equal input of viral genomes. NiV/VSV pseudotyped virions expressing NiV G alone were used as the negative control. Averages and standard errors of the mean from 3 independent experiments are shown. (B and D) Western blot analysis of equal numbers of genomes of N1 and N4, respectively. NiV/VSV viral lysates show relative levels of NiV G and processed (F_1) and unprocessed (F_0) NiV F incorporation.

indicated significantly decreased levels of fusion pore formation (DSP fusion) compared to wild-type NiV F (Fig. 4C, striped bars). Contrarily, the hyperfusogenic L257A and S259A mutants yielded ~180% ($P \leq 0.01$) and ~155% ($P \leq 0.05$) DSP fusion, respectively (Fig. 4C, striped bars). When we analyzed the statistical correlation between F-triggering and fusion pore formation for the N4 region mutants (Fig. 4D), we observed a significant positive correlation ($P = 0.0216$). Furthermore, when we collectively analyzed the N1 and N4 region mutants, we observed an even higher significant positive correlation (Fig. 4E and F, $P = 0.0068$; $P = 0.0039$). These analyses suggest that the N1 and N4 regions affect F-triggering and therefore the subsequent downstream fusion pore formation steps.

Hypofusogenic N1 and N4 region mutants infect at wild-type levels using a pseudotyped virus system. The requirements for fusion pore formation and extensive fusion pore expansion, although driven by similar mechanisms, are different. While fusion pore formation is sufficient to allow the transport of the relatively small viral genome from a virion into a host cell, extensive fusion pore expansion is required to allow for syncytial formation (the pathological hallmark of henipaviral disease) (3, 4). To study these phenotypes, we performed well-established biosafety level 2 (BSL2) NiV pseudotyped viral entry assays in which NiV surface glycoproteins were pseudotyped onto a vesicular stomatitis virus (NiV/VSV) (22, 38, 43, 49, 53) (Fig. 5A and C). Vero cells were infected with equilibrated genome copies of NiV/VSV pseudotyped virions over a series of 10-fold dilutions. Twenty-four hours postinfection, infected Vero cells were lysed and incubated with *Renilla* luciferase substrate to determine levels of luminescence (a correlate of viral entry). Western blot analyses were performed to determine the levels of NiV G and NiV F incorporation onto the NiV/VSV pseudotyped virions (Fig. 5B and D). In the case of the N1 region mutants, both the hypofusogenic P221A mutant and the hyperfusogenic S223A mutant yielded wild-type levels of viral entry and were incorporated to similar levels (Fig. 5A). Therefore, the N1 P221A hypofusogenic and S223A hyperfusogenic mutants were able to infect cells at wild-type levels, likely due to the fusion pore formation capabilities of these two mutants (Fig. 4A).

Interestingly, the N4 region hypofusogenic D252A mutant yielded wild-type levels of viral entry and G and F incorporation into virions (Fig. 5C and D). Since this mutant was able to trigger F and had reduced levels of fusion pore formation, it appears that
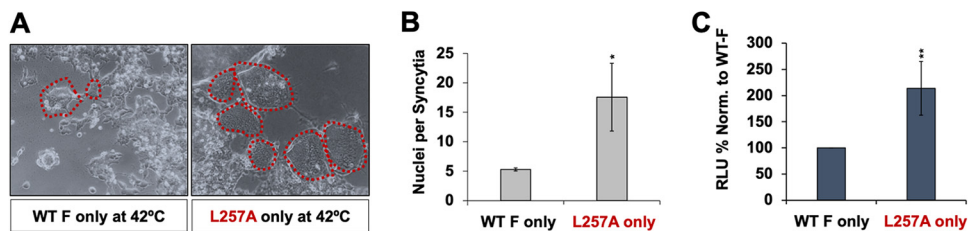
FIG 6 The N4 L257A mutant is able to fuse alone at 42°C. (A) Representative images of HEK 293T cells transfected with wild-type NiV F or the L257A mutant, in the absence of NiV G, and fused at 42°C. (B) Number of nuclei per syncytium yielded by wild-type F versus the L257A mutant. A total of ≥10 syncytia/transfected well were analyzed for both wild-type F and the L247A mutant alone. Data are averages and SDs from at least 3 independent experiments. Statistically significant differences, as determined by two-sample, two-tailed t tests, are marked with an asterisk: *, $P \leq 0.05$ (C) Dual split protein fusion assay performed at 42°C with 36-h effector and target cell overlay. RLU were normalized to WT F alone. Data are averages and SDs from 4 independent experiments. Statistically significant differences, as determined by one-sample, two-tailed t test, are marked with asterisks: **, $P \leq 0.01$.

the level of fusion pore formation for the L252A mutant is sufficient for entry of the relatively small viral genomes, but not sufficient for syncytium formation (moving of nuclei between fusing cells). Conversely, the N4 hyperfusogenic L257A mutant had decreased levels of viral entry, likely due to the low levels of incorporation into NiV/VSV glycoproteins into the pseudotyped virions (Fig. 5C and D).

The hyperfusogenic N4 region L257A mutant is able to induce formation of fusion pores and small syncytial pockets in the absence of NiV G at 42°C. As aforementioned, the L257A mutant had slightly decreased binding of conformational prefusion F MAbs 66 and 92 (Fig. 3D). The L257A NiV F mutant underwent about 70% enhanced levels of F-triggering and fusion pore formation (Fig. 4C). Furthermore, the L257A mutant displayed an ~6-fold increase in its syncytial fusion level compared to wild-type NiV F (Fig. 2C and D). Taking all these observations into account, we hypothesized that the L257A mutant may be in a more easily triggered state. To test this hypothesis, we performed both syncytial and DSP fusion assays at the elevated temperature of 42°C. For syncytial assays, HEK 293T cells were transfected with wild-type NiV F alone or the N4 L257A mutant alone (in the absence of NiV G) at 37°C initially. After 24 h posttransfection, cells were then moved to 42°C for an additional 96 h and analyzed by microscopy (Fig. 6A and B) (43, 54–56). We observed a level of wild-type NiV F syncytium formation of ~5 nuclei per syncytium (Fig. 6A and B). Remarkably, the N4 hyperfusogenic L257A NiV F mutant had syncytium formation levels about 3-fold higher (~17 nuclei per syncytium, $P \leq 0.05$ [Fig. 6A and B]). Quantitative DSP assays were also used to confirm results from the syncytial assay: the L257A NiV F mutant had fusion pore formation at ~2-fold higher levels when relative light units (RLU) were normalized to wild-type NiV F ($P \leq 0.01$ [Fig. 6C]) Therefore, at elevated temperatures, the L257A mutant was able to fuse in the absence of NiV G, suggesting that this residue in the N4 region is important for modulating F-triggering and cell-cell fusion, likely via fusion pore expansion, as well as F thermostability.

N1 and N4 region fusion mutants reveal that NiV F-G interaction dissociation is linked to F triggering. We and others have previously reported a receptor-induced dissociation of the attachment (H or G) and F glycoproteins during paramyxoviral membrane fusion (12, 36, 57). Furthermore, we reported a negative correlation between NiV F fusogenicity and F-G avidity interactions, suggesting that the F-G dissociation event is crucial during the membrane fusion process (22, 43, 45, 51, 53, 58). Using coimmunoprecipitation assays, we determined the levels of F-G interactions in cells that have largely undergone fusion. HEK 293T cells were cotransfected with wild-type NiV G and NiV F (wild type or N1 or N4 mutants). After 24 h, cells were collected and lysed, and F was immunoprecipitated. Both cell lysates and co-IP eluates were separated by SDS-PAGE (Fig. 7). Levels of F-G interaction or avidity were calculated using quantitative Western blot analyses. We found that in the case of the NiV F N1 region
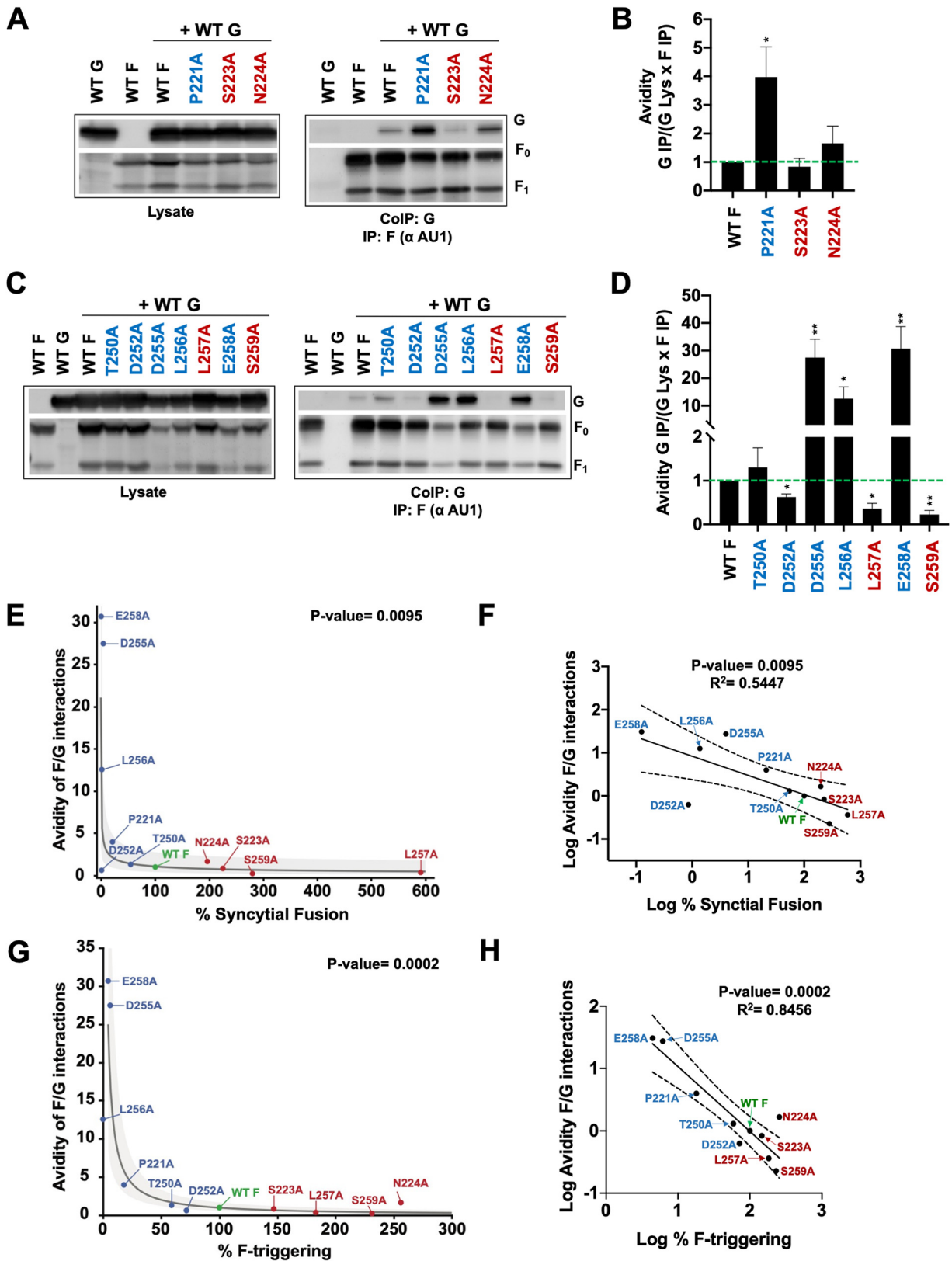
FIG 7 NiV-G associations are altered for some NiV F N1 and N4 fusion mutants. (A) Cell lysates (left) transfected with wild-type NiV G and NiV F (wild type or N1 region mutants) and co-IP (right). NiV F was pulled down using protein G coupled with rabbit anti-AU1. Associated NiV G was coimmunoprecipitated. (B) N1 mutant F/G co-IP values (relative avidities) were determined by dividing G IP by (G Lys × F IP), as previously performed to account for G and F expression and F IP capabilities (38, 49, 58, 63). Avidity values were normalized to wild-type

(Continued on next page)

mutants, the P221A hypofusogenic mutant had significantly increased levels of NiV F-G association compared to wild-type NiV F ($P \leq 0.05$ [Fig. 7A and B]). In contrast, the N1 hyperfusogenic S223A and N224A mutants have no significant difference in F-G association levels compared to wild-type NiV F (Fig. 7A and B). It is noteworthy that the apparent slight increase observed in N224A mutant interaction with NiV G (Fig. 7A and B) was found to be statistically nonsignificant.

In the N4 region, the hypofusogenic D255A ($P \leq 0.01$), L256A ($P \leq 0.05$), and E258A ($P \leq 0.01$) mutants displayed strong F-G interactions (Fig. 7C and D). Conversely, the hyperfusogenic L257A ($P \leq 0.05$) and S259A ($P \leq 0.01$) mutants displayed decreased F-G interactions (Fig. 7C and D). Interestingly, the hypofusogenic D252A mutant displayed decreased F-G avidity ($P \leq 0.05$ [Fig. 7C and D]). On a plot of percentage of syncytial fusion versus F-G interaction avidities for both the N1 and N4 hypo- and hyperfusogenic mutants, the data points appear to be distributed along an exponential dissociation trend (Fig. 7E). Indeed, a simple linear regression analysis indicated that a linear correlation is not an adequate model for our data and parameters ($R^2 = 0.217$, root mean square error [RMSE] = 10.57, $P = 0.1484 > 0.05$ [plot not shown]). The root mean square error is the standard deviation of the residuals (error in the prediction of the fit) and is a good measure of how far the data points are from the regression line. A log transformation of the percentage of syncytial fusion improved the fit parameters toward a more significant correlation ($R^2 = 0.530$, RMSE = 8.18, $P = 0.0110$ [plot not shown]). However, a log transformation of the avidity of F-G interactions further refined the quality of the fit parameters ($R^2 = 0.545$, RMSE = 0.52, $P = 0.0095$ [Fig. 7F]), particularly the RMSE and P values, indicating that this was a best fit model for our data.

To further understand how F-G interaction avidity and fusion correlate, we plotted one of the fusion steps, F-triggering, against F-G interaction avidities. Again, we observed that the data points appeared to be distributed along an exponential dissociation trend (Fig. 7G). Again, we first conducted a simple linear regression on the data and obtained very poor fit results ($R^2 = 0.390$, RMSE = 9.33, $P = 0.04$ [plot not shown]). However, a regression using a log transformation of F-triggering improved the fit to a significant degree ($R^2 = 0.781$, RMSE = 5.86, $P = 0.0007$ [plot not shown]), but failed to reduce the spread of the residuals enough. Adding a log transformation of the avidity of F-G interactions once again greatly refined the quality and significance of the fit parameters ($R^2 = 0.846$, RMSE = 0.30, $P = 0.0002$ [Fig. 7H]) and produced a model much more bound to the data. In both cases—avidity of F-G interactions versus percentage of F-triggering or versus percentage of syncytial fusion—the fit was greatly improved by the introduction of the log transformation of avidity as opposed to only the log transformation of percentage of F-triggering or percentage of syncytial fusion. This consistency supports the notion that the avidity of F-G interactions behaves exponentially instead of as a linear parameter.

Models for N1 and N4 region mechanism of F-triggering. To further understand the role of the N1 region in F-triggering, we analyzed the prefusion NiV F crystal structure (Fig. 8B to E). Interestingly, residue P221 interacts with HR3 (specifically amino acid I90), a region we recently reported to modulate F-triggering (Fig. 8B and C) (38).

FIG 7 Legend (Continued)
NiV F. The average from six experiments is shown, with error bars indicating the standard error of the mean. Statistically significant differences, as determined with a one-sample Student's t test, are marked with an asterisk: *, $P \leq 0.05$. (C) Cell lysates (left) transfected with wild-type NiV G and NiV F (wild type or N4 region mutants) and co-IP (right), similarly to panel A. (D) Avidities of F-G interactions for N4 mutants were determined by dividing G IP by (G Lys $\times$ F IP) and normalized to wild-type NiV F. The average from five experiments is shown, with error bars indicating the standard error of the mean. Statistically significant differences, as determined by a one-sample Student's t test, are marked with asterisks: *, $P \leq 0.05$; **, $P \leq 0.01$. (E) F-G interaction avidities plotted against percentage of syncytial fusion for the N1 and N4 region mutants. The gray line is the log transformation fit to the data, and the shaded area is the 95% confidence interval for the fit. (F) Plot of log avidity versus log percentage of syncytial fusion for N1 and N4 region mutants with 95% confidence interval for the fit. (G) F-G interaction avidities plotted against percentage of F-triggering for the N1 and N4 region mutants. The gray line is the log transformation fit to the data, and the shaded area is the 95% confidence interval for the fit. (F) Plot of log avidity versus log percentage of F-triggering for the N1 and N4 region mutants with 95% confidence interval for the fit.
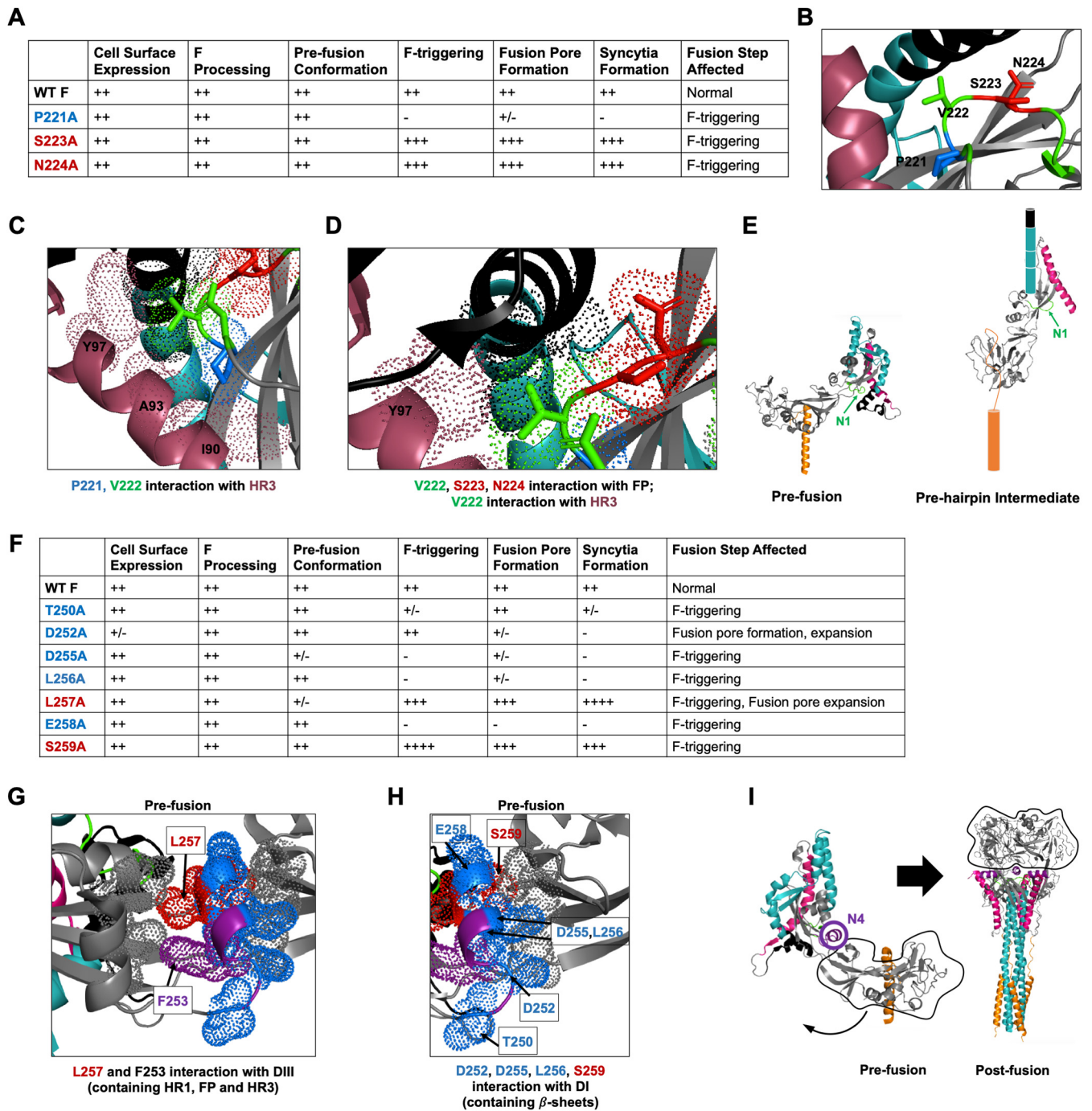
FIG 8 NiV F N1 and N4 mechanism models. (A) Summary of observed phenotypes of the N1 region mutants. ++ indicates wild-type F levels, − and +/− indicate a reduction, and +++ indicates an increase in the observed phenotype. (B) N1 with highlighted hyperfusogenic (red) and hypofusogenic (blue) mutants and V222 in close association with the FP, HR1, and HR3 (saturated magenta). (C) Space-filling model shows the P221 amino acid interacting with HR3 (saturated magenta). (D) Space-filling model depicts residues V222, S223, and N224 interacting with the FP (black). (E) Illustration of the N1 region playing a role in stabilizing F and initial release of the fusion peptide. (F) Summary of observed phenotypes of the N4 region mutants. (G) Space-filling model of N4 with highlighted hyperfusogenic (red) and hypofusogenic (blue) mutants, showing the L257 amino acid interacting with the DIII domain of F that contains HR1, FP, and HR3. (H) Space-filling model that shows D252, D255, L256, and S259 amino acids interacting with the DI domain of F that contains β-sheets. (I) Model of N4 playing a role as a stability core and which aids in shifting the DI during transition to the postfusion 6HB.

Residues S223 and N224 interface with the fusion peptide (Fig. 8B and D). Residue V222 is at an interface between the fusion peptide and the HR3 region (Fig. 8B and D). Based on our collective summarized findings (Fig. 8A) and these structural elements, we propose a model in which the N1 region plays an important role in proper folding

and in holding of the F protein in its prefusion conformation, as well as in its release from this prefusion conformation (Fig. 8B and D). Supporting this postulate, the V222A mutant had no total expression or CSE detected (Fig. 3A and Fig. 2A).

To further understand the role of the N4 region in the context of the biological functions (Fig. 8F), we analyzed the positions of key N4 residues within the prefusion NiV F crystal structure (Fig. 8G and H). Interestingly, the hyperfusogenic L257A mutant is located strictly on the opposing side of the N4 helix that contains all of the hypofusogenic mutants and interacts with the DIII domain of F, which contains the HR1, FP, and HR3 regions (Fig. 8G and H). Thus, we propose a conceivable model in which L257 is important for holding the prefusion structure together, and propose that the shorter alanine side-chain substitution in the L257A mutant could result in readily triggering F. The side of the helix that contains the hypofusogenic N4 mutants interacts with the DI domain β-sheets (Fig. 8H). Moreover, given the location of the N4 region within the F monomer (Fig. 8I), the N4 helix may function as a stability core between the high-energy metastable prefusion F and functions in modulating the movement of the DI region during transition to the postfusion 6HB (Fig. 8I).

Comparative analyses of N1 and N4 regions' primary sequences, locations, and configurations show similarity in other henipaviruses and paramyxoviruses. To assess whether our overall findings may apply to other henipaviruses and paramyxoviruses, protein sequence alignments and protein structure homology analyses were performed for the N1 and N4 regions (Fig. 9). The N1 primary amino acid sequence alignments between henipaviruses NiV, Hendra virus (HeV), Kumasi virus (KuV), and Cedar virus (CeV) revealed the N1 region has a high degree of similarity (Fig. 9A). Among paramyxoviruses, however, only a few amino acids are conserved in NiV F, PIV5 F, NDV F, measles virus (MeV) F, and canine distemper virus (CDV) F (Fig. 9B). Notably, the P221 residue has a high degree of conservation. The N1 structure and location near the FP, HR1, and HR3 are also well conserved among paramyxoviruses (Fig. 9C). Similarly, the N4 primary residue sequence is well conserved among henipaviruses (Fig. 9D). Important residues within the N4 region (D252, L256, L257, and S259) are similarly conserved among paramyxoviruses (Fig. 9E). Moreover, the secondary structure and location of the N4 region are maintained in paramyxoviruses (Fig. 9F). Due to these observations, the N1 and N4 region functions may be conserved in other henipaviral and paramyxoviral F proteins.

DISCUSSION

The N1 and N4 regions of NiV F and of other paramyxoviral F proteins remain largely understudied. Our present study is the first to show a function for the NiV F N1 region in modulating an early step of the fusion cascade, F-triggering, via alanine scanning mutagenesis and an array of functional assays (Fig. 8A). We were most interested in mutants that had defects in cell-cell fusion but had wild-type levels of CSE. Specifically, we identified three N1 residues that had an effect on modulation of fusogenicity, as shown by the P221A, S223A, and N224A mutants, and more specifically on an early F-triggering step (Fig. 8A). We verified that effects on fusion and F-triggering were not due to changes in F processing or differences in gross F conformations. Furthermore, the N1 early F-triggering effect dictated the observed phenotype of downstream steps, such as fusion pore formation and expansion (syncytium formation). In fact, when we plotted N1 F-triggering against fusion pore formation (along with N4 mutants), we observed a significant positive correlation between these two parameters. We recently reported on this F-triggering–fusion pore formation relationship with HR3, another region involved in F-triggering (38). Thus, the N1 region is likely involved in F-triggering (Fig. 8A), likely modulating the release of the fusion peptide, in conjunction with HR1 and HR3 (Fig. 8C to E). The N1 function may be conserved across henipaviruses and likely paramyxoviruses, as the N1 locality is conserved across several paramyxoviral fusion proteins (Fig. 9C).

We created NiV/VSV pseudotyped virions and measured their viral entry levels, as viral entry requires a small fusion pore to form and mildly expand enough to allow for
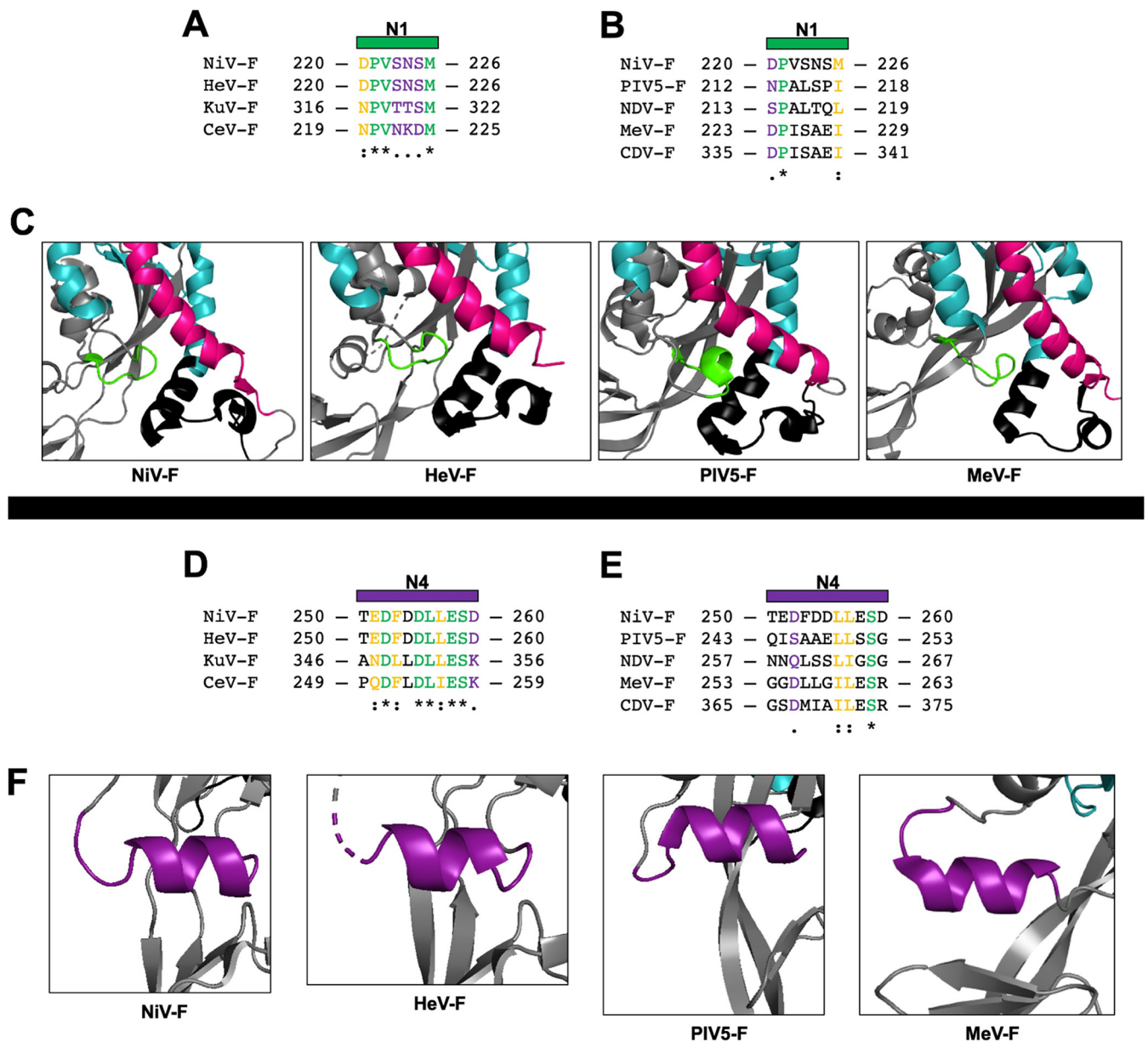
A

			N1		
NiV-F	220	—	DPVSNSM	—	226
HeV-F	220	—	DPVSNSM	—	226
KuV-F	316	—	NPVTTSM	—	322
CeV-F	219	—	NPVNKDM	—	225
			:**...*		

B

			N1		
NiV-F	220	—	DPVSNSM	—	226
PIV5-F	212	—	NPALSPI	—	218
NDV-F	213	—	SPALTQL	—	219
MeV-F	223	—	DPISAEI	—	229
CDV-F	335	—	DPISAEI	—	341
			.* :		

C

NiV-F HeV-F PIV5-F MeV-F

D

			N4		
NiV-F	250	—	TEDFDDLLESD	—	260
HeV-F	250	—	TEDFDDLLESD	—	260
KuV-F	346	—	ANDLLDLLESK	—	356
CeV-F	249	—	PQDFLDLIESK	—	259
			:*: **:**.		

E

			N4		
NiV-F	250	—	TEDFDDLLESD	—	260
PIV5-F	243	—	QISAAELLSSG	—	253
NDV-F	257	—	NNQLSSLIGSG	—	267
MeV-F	253	—	GGDLLGILESR	—	263
CDV-F	365	—	GSDMIAILESR	—	375
			. :: *		

F

NiV-F HeV-F PIV5-F MeV-F

FIG 9 N1 and N4 region sequence and structural homology. Sequence alignment of the portion of N1 in close association to the FP, HR1, and HR3 regions between NiV F and F of other henipaviruses (A) or between NiV F and F of other paramyxoviruses (B). (C) Structural positioning of the N1 region in the F prefusion structures among paramyxoviruses NiV, HeV, MeV, and PIV5, depicting the HR1 domain (teal), the FP domain (black), and the HR3 domain (magenta) (PDB accession codes 5EVM, 5EJB, 5YXW, and 4WSG). Sequence alignment of the portion of the N4 region between NiV F and F of other henipaviruses (D) or between NiV F and F of other paramyxoviruses (E). (F) Structural homology of the N4 region among paramyxoviruses in the prefusion conformation. The residues are either identical (*), very similar (:), or had similar residue side chains (.). PIV5 F was from the W3 strain, and MeV F was from the Ichinose-B95a strain. NDV, Newcastle disease virus; CDV, canine distemper virus.

viral genomes to enter the cell. N1 region P221A and S223A mutants yielded wild-type levels of viral entry, indicating that these mutants are able to form sufficient fusion pores. This is congruent with our DSP fusion pore formation assay data, as the P221A mutant was still able to form low levels of fusion pores (Fig. 4A). These findings suggest that as long as some fusion pores are able to form, cell content or viral genomes are able to enter the target host cells.

This study is also the first to show a role for the N4 NiV F region in early F-triggering, late fusion pore expansion steps, and F thermostability (Fig. 4 and 6). We were most interested in mutants that had defects in cell-cell fusion but had wild-type levels of CSE, and we also included the D252A mutant in our analysis, as it displayed only a

slight reduction in cell surface expression but no syncytium formation. We verified that effects on fusion and F-triggering were not due to changes in F processing or differences in gross F conformations, although D255A and L257A mutants had slightly lower binding to prefusion conformation MAbs 92 and 66, indicating that these mutants may be in a slightly different conformation that is less able to be triggered (D255A) or more easily triggered (L257A). Interestingly, the D252A mutant, which yielded no syncytia, was still able to be triggered and form fusion pores, indicating a defect post-fusion pore formation, such as in fusion pore expansion. Conversely, the L257A mutant yielded higher levels of F-triggering and fusion pore formation (both about ~1.8-fold over the wild type) but ~6-fold-higher levels of syncytium formation, suggesting an enhancement in fusion pore expansion. Overall, we have determined that N4 affects early F-triggering and late fusion pore expansion steps, as observed by effects on syncytium formation (Fig. 8F). We have also identified specific residues in the N4 region that are positively or negatively modulating these various phenotypes. We speculate that these functions may be conserved across henipaviruses and likely paramyxoviruses, as the N4 region structure is conserved across several paramyxoviral fusion proteins (Fig. 9F).

Consistent with this notion, the L257A mutant, which had lower binding of prefusion conformation MAbs 66 and 92, was able to yield fusion in the absence of G at 42°C (Fig. 6). This a novel phenotype among henipaviruses. Overall, these data suggest a role of the N4 region, and specifically residue L257, in F thermostability. Furthermore, the N4 region has been found at trimer-trimer interfaces in the predicted F hexamer-of-trimer prefusion structure, and we speculate that through this higher-order structure, the N4 region may affect extensive fusion pore expansion steps (28). Additionally, we performed NiV/VSV pseudotyped viral entry assays, as relatively smaller fusion pores are sufficient to allow for viral genomes to enter the cell compared to those needed for syncytium formation. The hypofusogenic N4 D252A mutant was able to infect Vero cells to wild-type levels, consistent with the fusion pore capabilities of this mutant despite the lack of syncytial formation. The hyperfusogenic L257A mutant yielded decreased viral entry, although this was likely due to the low levels of incorporation of L257A (Fig. 5C and D) (38, 53).

There are several variations of the paramyxoviral glycoprotein interaction models, which include the association and dissociation models of interactions, as well as more complex models (35). Paramyxoviruses containing the HN attachment protein typically follow variations of the association model in which HN and F interact to trigger fusion. On the other hand, paramyxoviruses containing the H or G attachment proteins follow variations of the dissociation model, whereby H/G and F interact prior to receptor binding and relatively dissociate upon F-triggering and subsequent steps. Supporting the dissociation model, we and others have shown that the fusogenic capacities of henipaviruses and MeV mutants inversely correlate with the avidity of interactions between F and the attachment glycoprotein (22, 36, 43, 51, 53, 57–59). When we examined avidity versus percentage of syncytial fusion of the N1 and N4 mutants collectively, we observed an exponential trend between these parameters (Fig. 7E). This exponential relationship was stronger when we plotted log F-G avidity against log F-triggering (Fig. 7G). Specifically, mutants substantially defective in F-triggering had strong interactions with G, and mutants with higher F-triggering capacities had decreased avidity with G. Therefore, it is likely a substantial level of F-G dissociation is important for F-triggering to occur effectively. In other words, F-triggering only happens or changes significantly when G-F interactions are low enough. In a biological sense, our data and correlation analyses show that as F and G dissociate (or their interactions decrease), F-triggering (and syncytial fusion) increases, but the significant increase in F-triggering (and syncytial fusion) only occurs when F and G are sufficiently dissociated (low avidity). This observation further supports a version of the F-G dissociation model of F-G interactions and indicates two defined steps linked in the membrane fusion process: F-G dissociation and F-triggering. This inverse correlation between F-G interactions and F-

triggering is novel and supports the notion that F-G dissociation is crucial at the early F-triggering step(s) of the fusion cascade.

Interestingly, the hypofusogenic D252A mutant yielded decreased F-G interaction, wild-type F-triggering capabilities, and a lack of syncytium formation (Fig. 8F). Another hypofusogenic mutant we previously reported (the K98A mutant in the HR3 region of NiV F) had a similar phenotype of wild-type F-triggering levels, with decreased syncytial formation and decreased F-G interactions (38). This suggests F-G interactions may play a role beyond that of F-triggering and in the extensive fusion pore expansion necessary for syncytium formation but not viral entry. It is important to note here that both of these mutants are found in regions of the F protein that participate in predicted hexamer-of-trimer interfaces (28). Thus, we postulate that G interactions with the hexamer of trimers may be important for extensive fusion pore expansion; however, further experimentation will be required to test this hypothesis.

Previously, Plemper et al. examined a cavity in the postfusion model of the MeV F containing a V94 residue (a residue located in MeV F HR3 region that differs between wild-type and attenuated Edmonston strains of MeV) surrounded by specific residues from the analogous MeV N1 and N4 region (60, 61). Mutating residues within this cavity resulted in defects in proper F processing and/or fusogenicity (61). Within this cavity, MeV P224 and I225 mutants (analogous to the NiV F P221 and V222 mutants) were shown to have defects in F processing but were still able to fuse (P224) or have no defect in processing or fusion (I225) (61). In contrast, the NiV F P221A mutant did not have defects in CSE, processing, or overall F conformation and yielded decreased syncytial formation due to decreased F-triggering. The V222A mutation resulted in completely abrogated F production. Thus, the mechanisms of fusion modulation for the N1 region may somewhat differ between henipaviruses and MeV. On the other hand, mutating MeV F residues L256 and L257 (aligned with NiV F D253 and D254) to charged residues resulted in decreases in surface expression and subsequent fusion (61). In our study, mutating the D253 N4 amino acid resulted in reduced total and cell surface expression. Thus, the N4 region may be involved in proper protein production for both NiV and MeV.

Overall, our findings support important roles for the N1 and N4 regions in modulating membrane fusion. Our data support the notion that NiV F contains several interacting "articulations" within its own structure that aid in the transition through several conformational changes within a trimer and between trimers in the predicted hexamer-of-trimer arrangements. Thus, it is likely that membrane fusion occurs through the sum of F protein's moving parts, utilizing the movement of HR1, HR2, and HR3, as well as the N1 and N4 regions. These functions may be conserved across paramyxoviruses, as the N1 and N4 regions are well conserved across henipaviruses and fairly conserved across paramyxoviral fusion proteins (Fig. 9) (28, 29, 32–34, 62). It is important to note here that NiV F N1 does not contain a helix, as observed in the PIV and NDV F structures; however, the location of N1 near HR1 and FP suggests a similar mechanism of action (Fig. 9). Our identification of the N1 and N4 NiV F regions as important factors for F-G avidities, which negatively correlated with F-triggering, is novel and confirms our original hypothesis based on structural analysis. Furthermore, relatively more surprisingly, we uncovered that the N4 region is likely also involved in extensive fusion pore expansion and F thermostability, adding to our understanding of the F rearrangements necessary during F-triggering and beyond, in later steps in the fusion cascade. This new understanding may in turn help the development of antivirals for the henipaviruses and paramyxoviruses.

MATERIALS AND METHODS

Cell culture. HEK 293T cells and Vero cells were obtained from the American Type Culture Collection (ATCC; Rockville, MD) and maintained in Dulbecco's modified Eagle's medium (DMEM) supplemented with 10% (vol/vol) fetal bovine serum (FBS) and maintained at 37°C and 5% CO_2.

Expression plasmids for mutants in the NiV F N1 and N4 regions. Previously, mammalian codon-optimized NiV G hemagglutinin (HA) C-terminus-tagged and NiV F AU1 C-terminus-tagged genes (F in Fig. 1B) were cloned within the KpnI and XhoI restriction sites of the pcDNA3.1(+) plasmid (14). Using

NiV F AU1 within the pcDNA3.1(+) vector as the template, scanning alanine point mutations were introduced in amino acids spanning aa 220–226 for the N1 region and aa 250–260 for the N4 region by site-directed mutagenesis using the QuikChange II XL kit (Agilent Technologies, CA). Mutants were verified by DNA sequencing. NiV F N1 and N4 region mutations were then inserted within the KpnI and XhoI restriction enzyme sites of the pCAGGS vector for improved protein expression (14, 43, 45).

Quantification of extensive fusion pore expansion by cell-cell fusion (syncytium formation). HEK 293T cells plated in six-well plates were transfected at 80 to 90% confluence with 2 μg/well of the NiV G wild type and NiV F wild type or NiV F N1 or N4 mutant in a 1:1 ratio. At 12 to 16 h posttransfection, cells were fixed with 1% paraformaldehyde (PFA), and syncytium formation was quantified by counting nuclei in fused cells per 200× field (with at least 5 fields counted per F analog). As previously defined, syncytia are qualified as four or more nuclei clearly visualized within a single shared cell membrane to exclude any mitotic events (22, 43, 45, 49, 53). For syncytial assays performed at 42°C, HEK 293T cells plated in 6-well plates were transfected at 80 to 90% confluence using of 3 μg/well of the NiV F wild type or NiV F N4 L257A mutant. At 24 h posttransfection, cells were moved from 37°C to 42°C and incubated for 4 days (96 h). Subsequently, cells were fixed with 1% PFA, and syncytium formation was quantified by counting nuclei in fused cells. Due to the few syncytial events and their uneven distribution, we examined the entire well for syncytium formation as opposed to our typical counting per 200× field.

Analysis of NiV F cell surface expression. HEK 293T cells plated in six-well plates were transfected at 80 to 90% confluence using 2 μg/well of NiV F wild type or mutant. At 16 to 18 h posttransfection, cells were collected and stained with primary anti-F polyclonal rabbit 834 or 835 antibody (which binds multiple epitopes in NiV F), at a 1:1,000 dilution in phosphate-buffered saline (PBS) containing 1% bovine albumin serum (BSA) for 1 h at 4°C. Production of anti-F serum from genetically immunized rabbits (injected with NiV F expression plasmids) was performed as previously described (22, 23, 43, 45). Bound primary antibody was detected with fluorophore-conjugated goat anti-rabbit antibodies at a dilution of 1:1,000 (Life Technologies). Cells were then fixed and analyzed by flow cytometry.

Total cell expression and percentage of processing via Western blotting. HEK 293T cells plated in six-well plates were transfected at 80 to 90% confluence with 2 μg/well NiV F wild type or mutant. At 36 h posttransfection, cells were lysed in 1× radioimmunoprecipitation assay (RIPA) buffer (EMD, Millipore, MA) combined with cOmplete Mini protease inhibitors (Roche, IN). Cell lysates were subjected to reducing SDS-PAGE Western blotting. NiV F proteins were probed using mouse anti-AU1 (1:500) antibody. Bound primary antibody was detected by fluorescently labeled secondary goat anti-mouse antibody (1:1,000). Proteins were detected, and the percentage of F processing was quantified using a ChemiDoc MP Imager system with Image Lab software (Bio-Rad, CA).

Analysis of NiV F conformational state via flow cytometry. Production of conformational anti-F monoclonal antibodies from hybridomas (MAbs 92 and 66) was previously described (45, 48). HEK 293T cells plated in six-well plates were transfected at 80 to 90% confluence with 2 μg/well of the NiV F wild type or mutant. At 16 h posttransfection, cells were collected and partitioned, and separate portions were stained with (i) primary anti-F rabbit serum 835 antibody at a 1:1,000 dilution, (ii) primary anti-F MAb 92 at a 1:1,000 dilution, or (iii) primary anti-F MAb 66 at a 1:1,000 dilution for 1 h at 4°C. Bound primary antibody was detected with fluorophore-conjugated goat anti-rabbit antibodies at a dilution of 1:1,000 (Life Technologies). Cells were then fixed and analyzed by flow cytometry. To control for differences in transfection efficiencies and differential expression from repeat experiments, Ab binding ratios were calculated by dividing the normalized (to wild type) mean fluorescence intensities obtained for the various Abs (92/835 and 66/835).

Quantification of F-triggering. F-triggering assays were performed as previously described (49, 50). HEK 293T cells were grown in 6-well plates and transfected at 80% confluence with 2 μg/well of NiV G and F (wild type or mutant) in a 1:3 ratio. Hypofusogenic N1 and N4 mutants were transfected for 10 to 14 h at 37°C. We've previously reported better F-triggering signal detection when cells were collected before substantial fusion (30 to 50% fusion) (38). Therefore, hyperfusogenic N1 and N4 mutants were initially transfected for 5 to 6 h at 37°C and then transferred to 32°C for an additional 4 to 8 h. Posttransfected cells were collected and partitioned into two separate portions to test for F cell surface expression (using the aforementioned labeling methods) and for F-triggering. F-triggering partitioned cells were incubated at 4°C for 1 h in the presence of 2 μM HR2-Cy5 peptide. Subsequently, cells were placed at 37°C for 30 min to allow F-triggering. Cells were then washed three times, and HR2-Cy5 peptide bound to triggered NiV F was detected by flow cytometry. We calculated levels of F-triggering based on levels of Cy5 signal and by normalizing to cell surface expression of F on the same group of cells (38, 49).

Quantification of fusion pore formation using a dual split protein fusion assay. HEK 293T cells were seeded in ViewPlate 96-well plates and transfected with wild-type NiV G, NiV F (wild type or mutant), and dual split protein (DSP$_{1-7}$) plasmids in a 2:6:4 ratio using 0.2 μg/well. Target cells were transfected with ephrin B2 plasmid and DSP$_{8-11}$. Ten to 12 h posttransfection, both effector and target cells were washed with PBS and incubated with live EnduRen live-cell substrate (Promega, WI) according to the manufacturer's instructions. Target cells were then lifted and mixed with effector cells in a 1:1 ratio and incubated for 8 h at 37°C. Luciferase activity as a measure of fusion pore formation was then analyzed 8 h postoverlay and normalized to wild-type NiV F (set as 100%) as previously described (37, 38, 49, 52). For quantitative dual split protein fusion assays performed at 42°C, HEK 293T cells were transfected with NiV F (wild type or the L257A N4 mutant) and DSP$_{1-7}$ in a 2:1 ratio using 0.2 μg/well. Target cells were transfected as aforementioned. After an initial 24-h transfection at 37°C, target cells were washed, lifted and overlaid onto effector cells, and incubated at 42°C for 36 h. After this overlay period,

cells were washed, loaded, and incubated with EnduRen following the manufacturer's specifications. Luciferase activity as a measure of fusion pore formation was then analyzed and normalized to wild-type NiV F alone (set as 100%).

Pseudotyped viral entry assay. NiV surface glycoproteins were pseudotyped onto a vesicular stomatitis virus (VSV) as previously described (22, 38, 43, 49, 53). HEK 293T cells were seeded on 10-cm plates and transfected at 80 to 90% confluence with wild-type NiV G and NiV F (wild type or mutant) in a 1:3 ratio using 8 μg/plate. Ten to 12 h posttransfection, cells were subsequently infected with a recombinant VSV expressing the *Renilla* luciferase reporter gene in place of the native VSV G gene (VSV-ΔG-rLuc). Generated NiV/VSV pseudotyped virions were purified over a 20% sucrose cushion. Genome copy numbers of isolated NiV/VSV pseudotyped virions were quantified by primarily extracting viral RNA using the E.Z.NA Viral RNA kit (Omega Bio-tek, GA) and subsequent quantitative reverse transcription-PCR (RT-qPCR) utilizing UltraPlex 1-Step (Quantabio, MA) with a TaqMan Ind-1 spec probe.

To assess infectivity profiles of NiV/VSV pseudotyped virions, Vero cells were plated in 96-well plates for 8 to 10 h and subsequently infected with genome-equilibrated NiV/VSV pseudotyped virions in PBS supplemented with 1% fetal bovine serum (FBS) for 2 h at 37°C. Infections were done over a 5-fold viral dilution range (10^{-3} to 10^{-7}). At 24 h postinfection, Vero cells were lysed, and luciferase activity was measured as relative light units (RLU) with a *Renilla* luciferase activity detection kit (Promega, WI) and a Tecan Spark plate reader (Tecan Group, Ltd., Switzerland). RLU were plotted against serial dilutions (22, 43, 49, 53).

Coimmunoprecipitation of NiV G with NiV F via Western blot analysis. HEK 293T cells were grown in 6-well plates and transfected with 3 μg/well of HA-tagged NiV G and AU1-tagged NiV F (wild-type or mutant) in a 1:1 ratio using Lipofectamine 2000. At 24 h posttransfection, cells were lysed with 1$\times$ RIPA buffer (EMD, Millipore, MA) combined with cOmplete Mini protease inhibitors (Roche, IN). Subsequently, cell lysates were incubated with protein G beads coupled with rabbit anti-AU1. MACS magnetic μ columns (Miltenyi, Germany) were prepared by washing with lysis/wash buffer (0.025 M Tris, 0.15 M NaCl, 0.001 M EDTA, 1% NP-40). Lysates were added to and passed through the μ column, and beads were washed. Bound immunoprecipitated protein was eluted and analyzed by 10% SDS-PAGE Western blotting. NiV F was pulled down using protein G coupled with rabbit anti-AU1. Associated NiV G was coimmunoprecipitated and blotted with anti-HA Ab conjugated to phycoerythrin (PE). NiV F was detected using mouse anti-AU1 plus goat anti-mouse conjugated to Alexa Fluor 488. Bio-Rad Image software was used to measure the densitometry of NiV G and F bands. A separate lysate portion was set aside for direct immunoblot analysis without immunoprecipitation. NiV G avidity or interaction quantification was performed as previously described (22, 23, 53, 58, 63).

Statistical analyses. Statistical analyses were performed using GraphPad Prism, versions 8 and 9. We performed one-sample, two-tailed t tests for comparisons between the wild type and N1/N4 NiV F mutant analogs. Wild-type NiV F was normalized (always set as 100% or 1.0, depending on the analysis). We performed unpaired, two-sample, two-tailed t tests for comparisons between N1/N4 NiV F mutants and wild-type NiV F processing levels and NiV/VSV pseudotyped viral entry assays and 42°C syncytial assays. Correlation analyses were performed using GraphPad Prism, version 8, and JMP, version 15. Nonsignificant differences ($P > 0.05$) are unmarked. * denotes a significant difference ($P \leq 0.05$), ** denotes a very significant difference ($P \leq 0.01$), and *** and **** denote very high significant differences ($P \leq 0.001$ and $P \leq 0.0001$, respectively).

REFERENCES

1. WHO. 2020. Prioritizing diseases for research and development in emergency contexts. https://www.who.int/activities/prioritizing-diseases-for-research-and-development-in-emergency-contexts.
2. Thakur N, Bailey D. 2019. Advances in diagnostics, vaccines and therapeutics for Nipah virus. Microbes Infect 21:278–286. https://doi.org/10.1016/j.micinf.2019.02.002.
3. Wong KT, Grosjean I, Brisson C, Blanquier B, Fevre-Montange M, Bernard A, Loth P, Georges-Courbot MC, Chevallier M, Akaoka H, Marianneau P, Lam SK, Wild TF, Deubel V. 2003. A golden hamster model for human acute Nipah virus infection. Am J Pathol 163:2127–2137. https://doi.org/10.1016/S0002-9440(10)63569-9.
4. Wong KT, Shieh WJ, Kumar S, Norain K, Abdullah W, Guarner J, Goldsmith CS, Chua KB, Lam SK, Tan CT, Goh KJ, Chong HT, Jusoh R, Rollin PE, Ksiazek TG, Zaki SR, Nipah Virus Pathology Working Group. 2002. Nipah

virus infection: pathology and pathogenesis of an emerging paramyxoviral zoonosis. Am J Pathol 161:2153–2167. https://doi.org/10.1016/S0002-9440(10)64493-8.
5. Ching PK, de los Reyes VC, Sucaldito MN, Tayag E, Columna-Vingno AB, Malbas FF, Jr, Bolo GC, Jr, Sejvar JJ, Eagles D, Playford G, Dueger E, Kaku Y, Morikawa S, Kuroda M, Marsh GA, McCullough S, Foxwell AR. 2015. Outbreak of henipavirus infection, Philippines, 2014. Emerg Infect Dis 21:328–331. https://doi.org/10.3201/eid2102.141433.
6. Chua KB, Bellini WJ, Rota PA, Harcourt BH, Tamin A, Lam SK, Ksiazek TG, Rollin PE, Zaki SR, Shieh W, Goldsmith CS, Gubler DJ, Roehrig JT, Eaton B, Gould AR, Olson J, Field H, Daniels P, Ling AE, Peters CJ, Anderson LJ, Mahy BW. 2000. Nipah virus: a recently emergent deadly paramyxovirus. Science 288:1432–1435. https://doi.org/10.1126/science.288.5470.1432.

7. Broder CC, Weir DL, Reid PA. 2016. Hendra virus and Nipah virus animal vaccines. Vaccine 34:3525–3534. https://doi.org/10.1016/j.vaccine.2016.03.075.

8. Butler D. 2017. Billion-dollar project aims to prep vaccines before epidemics hit. Nature 541:444–445. https://doi.org/10.1038/nature.2017.21329.

9. Aguilar HC, Lee B. 2011. Emerging paramyxoviruses: molecular mechanisms and antiviral strategies. Expert Rev Mol Med 13:e6. https://doi.org/10.1017/S1462399410001754.

10. Bose S, Jardetzky TS, Lamb RA. 2015. Timing is everything: fine-tuned molecular machines orchestrate paramyxovirus entry. Virology 479-480:518–531. https://doi.org/10.1016/j.virol.2015.02.037.

11. Bossart KN, Fusco DL, Broder CC. 2013. Paramyxovirus entry. Adv Exp Med Biol 790:95–127. https://doi.org/10.1007/978-1-4614-7651-1_6.

12. Chang A, Dutch RE. 2012. Paramyxovirus fusion and entry: multiple paths to a common end. Viruses 4:613–636. https://doi.org/10.3390/v4040613.

13. Jardetzky TS, Lamb RA. 2014. Activation of paramyxovirus membrane fusion and virus entry. Curr Opin Virol 5:24–33. https://doi.org/10.1016/j.coviro.2014.01.005.

14. Negrete OA, Levroney EL, Aguilar HC, Bertolotti-Ciarlet A, Nazarian R, Tajyar S, Lee B. 2005. EphrinB2 is the entry receptor for Nipah virus, an emergent deadly paramyxovirus. Nature 436:401–405. https://doi.org/10.1038/nature03838.

15. Negrete OA, Wolf MC, Aguilar HC, Enterlein S, Wang W, Muhlberger E, Su SV, Bertolotti-Ciarlet A, Flick R, Lee B. 2006. Two key residues in ephrinB3 are critical for its use as an alternative receptor for Nipah virus. PLoS Pathog 2:e7. https://doi.org/10.1371/journal.ppat.0020007.

16. Xu K, Rajashankar KR, Chan YP, Himanen JP, Broder CC, Nikolov DB. 2008. Host cell recognition by the henipaviruses: crystal structures of the Nipah G attachment glycoprotein and its complex with ephrin-B3. Proc Natl Acad Sci U S A 105:9953–9958. https://doi.org/10.1073/pnas.0804797105.

17. Lamb RA, Paterson RG, Jardetzky TS. 2006. Paramyxovirus membrane fusion: lessons from the F and HN atomic structures. Virology 344:30–37. https://doi.org/10.1016/j.virol.2005.09.007.

18. Morrison TG. 2003. Structure and function of a paramyxovirus fusion protein. Biochim Biophys Acta 1614:73–84. https://doi.org/10.1016/s0005-2736(03)00164-0.

19. Pager CT, Craft WW, Patch J, Dutch RE. 2006. A mature and fusogenic form of the Nipah virus fusion protein requires proteolytic processing by cathepsin L. Virology 346:251–257. https://doi.org/10.1016/j.virol.2006.01.007.

20. Diederich S, Dietzel E, Maisner A. 2009. Nipah virus fusion protein: influence of cleavage site mutations on the cleavability by cathepsin L, trypsin and furin. Virus Res 145:300–306. https://doi.org/10.1016/j.virusres.2009.07.020.

21. Diederich S, Sauerhering L, Weis M, Altmeppen H, Schaschke N, Reinheckel T, Erbar S, Maisner A. 2012. Activation of the Nipah virus fusion protein in MDCK cells is mediated by cathepsin B within the endosome-recycling compartment. J Virol 86:3736–3745. https://doi.org/10.1128/JVI.06628-11.

22. Liu Q, Stone JA, Bradel-Tretheway B, Dabundo J, Benavides Montano JA, Santos-Montanez J, Biering SB, Nicola AV, Iorio RM, Lu X, Aguilar HC. 2013. Unraveling a three-step spatiotemporal mechanism of triggering of receptor-induced Nipah virus fusion and cell entry. PLoS Pathog 9:e1003770. https://doi.org/10.1371/journal.ppat.1003770.

23. Liu Q, Bradel-Tretheway B, Monreal AI, Saludes JP, Lu X, Nicola AV, Aguilar HC. 2015. Nipah virus attachment glycoprotein stalk C-terminal region links receptor binding to fusion triggering. J Virol 89:1838–1850. https://doi.org/10.1128/JVI.02277-14.

24. Xu Y, Lou Z, Liu Y, Cole DK, Su N, Qin L, Li X, Bai Z, Rao Z, Gao GF. 2004. Crystallization and preliminary crystallographic analysis of the fusion core from two new zoonotic paramyxoviruses, Nipah virus and Hendra virus. Acta Crystallogr D Biol Crystallogr 60:1161–1164. https://doi.org/10.1107/S0907444904009515.

25. McGinnes L, Sergel T, Reitter J, Morrison T. 2001. Carbohydrate modifications of the NDV fusion protein heptad repeat domains influence maturation and fusion activity. Virology 283:332–342. https://doi.org/10.1006/viro.2001.0899.

26. Zhu J, Ding Y, Gao F, Wu T, Zhang CW, Tien P, Rao Z, Gao GF. 2003. Crystallization and preliminary X-ray crystallographic analysis of the trimer core from measles virus fusion protein. Acta Crystallogr D Biol Crystallogr 59:587–590. https://doi.org/10.1107/s0907444903001057.

27. Zhu J, Li P, Wu T, Gao F, Ding Y, Zhang CW, Rao Z, Gao GF, Tien P. 2003. Design and analysis of post-fusion 6-helix bundle of heptad repeat regions from Newcastle disease virus F protein. Protein Eng 16:373–379. https://doi.org/10.1093/protein/gzg041.

28. Xu K, Chan YP, Bradel-Tretheway B, Akyol-Ataman Z, Zhu Y, Dutta S, Yan L, Feng Y, Wang LF, Skiniotis G, Lee B, Zhou ZH, Broder CC, Aguilar HC, Nikolov DB. 2015. Crystal structure of the pre-fusion Nipah virus fusion glycoprotein reveals a novel hexamer-of-trimers assembly. PLoS Pathog 11:e1005322. https://doi.org/10.1371/journal.ppat.1005322.

29. Chen L, Gorman JJ, McKimm-Breschkin J, Lawrence LJ, Tulloch PA, Smith BJ, Colman PM, Lawrence MC. 2001. The structure of the fusion glycoprotein of Newcastle disease virus suggests a novel paradigm for the molecular mechanism of membrane fusion. Structure 9:255–266. https://doi.org/10.1016/s0969-2126(01)00581-0.

30. Yin HS, Paterson RG, Wen X, Lamb RA, Jardetzky TS. 2005. Structure of the uncleaved ectodomain of the paramyxovirus (hPIV3) fusion protein. Proc Natl Acad Sci U S A 102:9288–9293. https://doi.org/10.1073/pnas.0503989102.

31. Yin HS, Wen X, Paterson RG, Lamb RA, Jardetzky TS. 2006. Structure of the parainfluenza virus 5 F protein in its metastable, prefusion conformation. Nature 439:38–44. https://doi.org/10.1038/nature04322.

32. Hashiguchi T, Fukuda Y, Matsuoka R, Kuroda D, Kubota M, Shirogane Y, Watanabe S, Tsumoto K, Kohda D, Plemper RK, Yanagi Y. 2018. Structures of the prefusion form of measles virus fusion protein in complex with inhibitors. Proc Natl Acad Sci U S A 115:2496–2501. https://doi.org/10.1073/pnas.1718957115.

33. Welch BD, Liu Y, Kors CA, Leser GP, Jardetzky TS, Lamb RA. 2012. Structure of the cleavage-activated prefusion form of the parainfluenza virus 5 fusion protein. Proc Natl Acad Sci U S A 109:16672–16677. https://doi.org/10.1073/pnas.1213802109.

34. Wong JJ, Paterson RG, Lamb RA, Jardetzky TS. 2016. Structure and stabilization of the Hendra virus F glycoprotein in its prefusion form. Proc Natl Acad Sci U S A 113:1056–1061. https://doi.org/10.1073/pnas.1523303113.

35. Aguilar HC, Henderson BA, Zamora JL, Johnston GP. 2016. Paramyxovirus glycoproteins and the membrane fusion process. Curr Clin Microbiol Rep 3:142–154. https://doi.org/10.1007/s40588-016-0040-8.

36. Ader N, Brindley M, Avila M, Orvell C, Horvat B, Hiltensperger G, Schneider-Schaulies J, Vandevelde M, Zurbriggen A, Plemper RK, Plattet P. 2013. Mechanism for active membrane fusion triggering by morbillivirus attachment protein. J Virol 87:314–326. https://doi.org/10.1128/JVI.01826-12.

37. Brindley MA, Plattet P, Plemper RK. 2014. Efficient replication of a paramyxovirus independent of full zippering of the fusion protein six-helix bundle domain. Proc Natl Acad Sci U S A 111:E3795–E3804. https://doi.org/10.1073/pnas.1403609111.

38. Zamora JLR, Ortega V, Johnston GP, Li J, André NM, Monreal IA, Contreras EM, Whittaker GR, Aguilar HC. 2020. Third helical domain of the Nipah virus fusion glycoprotein modulates both early and late steps in the membrane fusion cascade. J Virol 94:e00644-20. https://doi.org/10.1128/JVI.00644-20.

39. Arnold K, Bordoli L, Kopp J, Schwede T. 2006. The SWISS-MODEL workspace: a web-based environment for protein structure homology modelling. Bioinformatics 22:195–201. https://doi.org/10.1093/bioinformatics/bti770.

40. Biasini M, Bienert S, Waterhouse A, Arnold K, Studer G, Schmidt T, Kiefer F, Gallo Cassarino T, Bertoni M, Bordoli L, Schwede T. 2014. SWISS-MODEL: modelling protein tertiary and quaternary structure using evolutionary information. Nucleic Acids Res 42:W252–W258. https://doi.org/10.1093/nar/gku340.

41. Bordoli L, Kiefer F, Arnold K, Benkert P, Battey J, Schwede T. 2009. Protein structure homology modeling using SWISS-MODEL workspace. Nat Protoc 4:1–13. https://doi.org/10.1038/nprot.2008.197.

42. Kiefer F, Arnold K, Künzli M, Bordoli L, Schwede T. 2009. The SWISS-MODEL Repository and associated resources. Nucleic Acids Res 37:D387–D392. https://doi.org/10.1093/nar/gkn750.

43. Aguilar HC, Matreyek KA, Filone CM, Hashimi ST, Levroney EL, Negrete OA, Bertolotti-Ciarlet A, Choi DY, McHardy I, Fulcher JA, Su SV, Wolf MC, Kohatsu L, Baum LG, Lee B. 2006. N-glycans on Nipah virus fusion protein protect against neutralization but reduce membrane fusion and viral entry. J Virol 80:4878–4889. https://doi.org/10.1128/JVI.80.10.4878-4889.2006.

44. Whitman SD, Dutch RE. 2007. Surface density of the Hendra G protein modulates Hendra F protein-promoted membrane fusion: role for Hendra G protein trafficking and degradation. Virology 363:419–429. https://doi.org/10.1016/j.virol.2007.01.029.

45. Aguilar HC, Matreyek KA, Choi DY, Filone CM, Young S, Lee B. 2007. Polybasic KKR motif in the cytoplasmic tail of Nipah virus fusion protein modulates

membrane fusion by inside-out signaling. J Virol 81:4520–4532. https://doi.org/10.1128/JVI.02205-06.

46. Aguilar HC, Ataman ZA, Aspericueta V, Fang AQ, Stroud M, Negrete OA, Kammerer RA, Lee B. 2009. A novel receptor-induced activation site in the Nipah virus attachment glycoprotein (G) involved in triggering the fusion glycoprotein (F). J Biol Chem 284:1628–1635. https://doi.org/10.1074/jbc.M807469200.

47. Diederich S, Thiel L, Maisner A. 2008. Role of endocytosis and cathepsin-mediated activation in Nipah virus entry. Virology 375:391–400. https://doi.org/10.1016/j.virol.2008.02.019.

48. Avanzato VA, Oguntuyo KY, Escalera-Zamudio M, Gutierrez B, Golden M, Kosakovsky Pond SL, Pryce R, Walter TS, Seow J, Doores KJ, Pybus OG, Munster VJ, Lee B, Bowden TA. 2019. A structural basis for antibody-mediated neutralization of Nipah virus reveals a site of vulnerability at the fusion glycoprotein apex. Proc Natl Acad Sci U S A 116:25057–25067. https://doi.org/10.1073/pnas.1912503116.

49. Bradel-Tretheway BG, Zamora JLR, Stone JA, Liu Q, Li J, Aguilar HC. 2019. Nipah and Hendra virus glycoproteins induce comparable homologous but distinct heterologous fusion phenotypes. J Virol 93:e00577-19. https://doi.org/10.1128/JVI.00577-19.

50. Aguilar HC, Aspericueta V, Robinson LR, Aanensen KE, Lee B. 2010. A quantitative and kinetic fusion protein-triggering assay can discern distinct steps in the Nipah virus membrane fusion cascade. J Virol 84:8033–8041. https://doi.org/10.1128/JVI.00469-10.

51. Biering SB, Huang A, Vu AT, Robinson LR, Bradel-Tretheway B, Choi E, Lee B, Aguilar HC. 2012. N-glycans on the Nipah virus attachment glycoprotein modulate fusion and viral entry as they protect against antibody neutralization. J Virol 86:11991–12002. https://doi.org/10.1128/JVI.01304-12.

52. Brindley MA, Suter R, Schestak I, Kiss G, Wright ER, Plemper RK. 2013. A stabilized headless measles virus attachment protein stalk efficiently triggers membrane fusion. J Virol 87:11693–11703. https://doi.org/10.1128/JVI.01945-13.

53. Stone JA, Nicola AV, Baum LG, Aguilar HC. 2016. Multiple novel functions of Henipavirus O-glycans: the first O-glycan functions identified in the paramyxovirus family. PLoS Pathog 12:e1005445. https://doi.org/10.1371/journal.ppat.1005445.

54. Millet JK, Goldstein ME, Labitt RN, Hsu HL, Daniel S, Whittaker GR. 2016. A camel-derived MERS-CoV with a variant spike protein cleavage site and distinct fusion activation properties. Emerg Microbes Infect 5:e126. https://doi.org/10.1038/emi.2016.125.

55. Sisk JM, Frieman MB, Machamer CE. 2018. Coronavirus S protein-induced fusion is blocked prior to hemifusion by Abl kinase inhibitors. J Gen Virol 99:619–630. https://doi.org/10.1099/jgv.0.001047.

56. Straus MR, Tang T, Lai AL, Flegel A, Bidon M, Freed JH, Daniel S, Whittaker GR. 2020. Ca^{2+} ions promote fusion of Middle East respiratory syndrome coronavirus with host cells and increase infectivity. J Virol 94:e00426-20. https://doi.org/10.1128/JVI.00426-20.

57. Bishop KA, Hickey AC, Khetawat D, Patch JR, Bossart KN, Zhu Z, Wang LF, Dimitrov DS, Broder CC. 2008. Residues in the stalk domain of the Hendra virus G glycoprotein modulate conformational changes associated with receptor binding. J Virol 82:11398–11409. https://doi.org/10.1128/JVI.02654-07.

58. Bradel-Tretheway BG, Liu Q, Stone JA, McInally S, Aguilar HC. 2015. Novel functions of Hendra virus G N-glycans and comparisons to Nipah virus. J Virol 89:7235–7247. https://doi.org/10.1128/JVI.00773-15.

59. Plemper RK, Hammond AL, Gerlier D, Fielding AK, Cattaneo R. 2002. Strength of envelope protein interaction modulates cytopathicity of measles virus. J Virol 76:5051–5061. https://doi.org/10.1128/jvi.76.10.5051-5061.2002.

60. Plemper RK, Compans RW. 2003. Mutations in the putative HR-C region of the measles virus F2 glycoprotein modulate syncytium formation. J Virol 77:4181–4190. https://doi.org/10.1128/jvi.77.7.4181-4190.2003.

61. Plemper RK, Lakdawala AS, Gernert KM, Snyder JP, Compans RW. 2003. Structural features of paramyxovirus F protein required for fusion initiation. Biochemistry 42:6645–6655. https://doi.org/10.1021/bi034385k.

62. Swanson K, Wen X, Leser GP, Paterson RG, Lamb RA, Jardetzky TS. 2010. Structure of the Newcastle disease virus F protein in the post-fusion conformation. Virology 402:372–379. https://doi.org/10.1016/j.virol.2010.03.050.

63. Stone JA, Vemulapati BM, Bradel-Tretheway B, Aguilar HC. 2016. Multiple strategies reveal a bidentate interaction between the Nipah virus attachment and fusion glycoproteins. J Virol 90:10762–10773. https://doi.org/10.1128/JVI.01469-16.